Chapter 5

Feasibility Study on the Design of a Dry First Wall

5.1 Objective

One of the most critical issues in a laser fusion reactor design is high heat and particle load on the chamber first wall. Especially if a dry wall is adopted for the chamber, its response to the pulse load can be a crucial factor that determines the feasibility of the plant system design. Thus the detailed analysis of the response of the dry first wall to the heat and particle load is necessary.

There are several factors that can lead to mass loss of a dry wall;

- surface melting due to temperature increase to its melting point
- deterioration in thermomechanical properties due to the change of surface morphology accompanied with temperature increase to threshold temperature
- fatigue failure due to cyclic thermal stress accompanied with temperature elevation
- overheating of the armor material caused by the reduction of convection between the armor and the structural material results from the deterioration of bonding between them due to cyclic thermal stress at the interface
- chemical and physical sputtering
- blistering and exfoliation due to helium accumulation
- deterioration of thermomechanical properties due to compositional change by chemical reactions

The first four factors are due to a heat load and remaining three factors are due to a particle load. Here temperature also greatly influences the effect of a particle load. Thus at first we evaluated the temporal temperature increase.

5.2 1-D thermal analysis

5.2.1 Model description

An IFE first wall is exposed to the irradiation of high energy X-rays and charged particles. The material exposed to such high heat and particle loads must have high melting point to avoid a melt layer loss. To suppress the temperature increase, high thermal conductivity, especially in high temperature region, is also required. Carbon and several refractory metals are known as the materials that satisfy the above requirements.

Caron does not melt but it sublimates around 3600 K. It is know to have a good thermal conductivity. It also has a merit of easiness in fabrication. Recently developed carbon fiber composites (CFCs) has a high mechanical strength comparable to metals and shows quite high thermal conductivity along a specific direction by adjusting fiber orientation. Thus CFCs is a most probable candidate of plasma facing components (PFCs) of ITER [41] and JT-60SA [42]. But carbon is easily eroded through a chemical reaction with hydrogen isotopes. It can be easily deposited on the wall with tritium. This co-deposition is a great safety issue in a fusion reactor. Then refractory metals are expected to be an alternative material. Among them, tungsten has the highest melting point in the whole materials (3680 K) and shows good thermal conductivity at high temperature regime. Thus tungsten is a strong candidate of PFCs for a commercial reactor. HAPL project also selected tungsten for the first wall material. Although silicon carbide (SiC) and its composites are also a candidate of PFCs, they still has a problem to fabricate large components and there is not sufficient data of its thermomechanical properties.

Therefore, in this study we selected tungsten for the first wall material. As shown in the following, however, only thin region close to the surface undergoes the large temperature elevation. Thus there is no need to use tungsten, one of the rare metals, for whole region of the first wall. Then it is considered to use tungsten for only heat protection and use another material to keep structural strength. We selected reduced-activate ferritic steel F82H (Fe-8Cr-2W) for the structural material because it also considered to be a most probable candidate for the structural material of a fusion plant and many experimental data are available.

Figure 5.1 describes the model used in this calculation. The thicknesses of tungsten and F82H are selected to be 1 mm and 3 mm. As already described in chapter 3, the first wall is assumed to be convectively cooled by 623 K pressurized supercritical water at the opposite side of tungsten bonded (here assuming convective heat transfer coefficient as 20 $kW/m^2 \cdot K$ regardless to the temperature of the water). Initially temperature of whole region is set to be 623K. In this study the chamber shape is

assumed to be a perfect sphere and it is considered that there is no remarkable effect to break symmetry of heat deposition. Thus we assumed the whole region of plasma facing side of the first wall is kept to be a uniform temperature and no radiation occurs from the surface. Then we assume adiabatic boundary condition for the opposite side of the first wall.

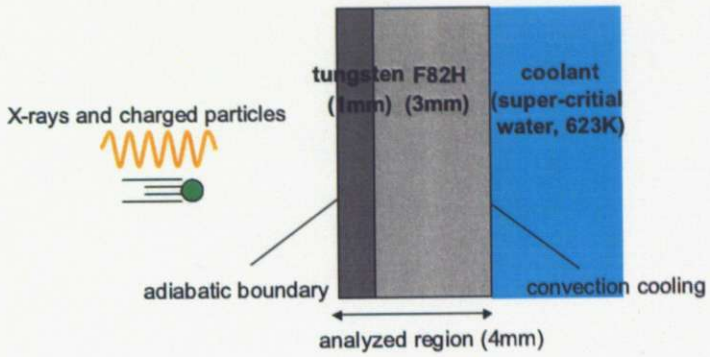

Fig. 5.1: Schematic view of the model used in the 1-D thermal analysis

With this model, temporal temperature evolution of the first wall can be calculated by solving one-dimensional thermal conduction equation:

$$\rho C(T)\frac{\partial T(x,t)}{\partial t} = \frac{\partial}{\partial x}\left(k(T)\frac{\partial T(x,t)}{\partial x}\right) + \dot{q}(x) \tag{5.1}$$

where ρ, C are the density and specific heat of the materials and k is thermal conductivity. Here temperature dependence of thermal properties was considered. The data of these thermal properties are obtained from reference [43, 44].

In Eq. (5.1), $\dot{q}(x)$ represents a volumetic heat generation due to X-rays and charged particles from the core plasma. Here we used the spectra data of X-rays and charged particles (proton, deuteron, triton, and carbon ion) obtained from the 1-D hydrodynamic simulation (described in the previous chapter). Here we consider time-of-flight expansion of the spectra. Figure 5.2 and 5.3 show the spectra of X-rays and charge particles used in this analysis. Heat deposition profile along the depth is calculated with photoabsorption coefficient [45] and ion stopping of the first wall materials. Stopping data is calculated by a SRIM (Stooping and Range of Ions in Materials) code [46].

5.2.2 Results and discussion

Figure 5.4 shows the temporal temperature evolution at various depths of the first wall during the first shot. Here we assume chamber radius to be 5.64 m according to the estimation result by a 0-D analysis model. One can see three peaks that coincide to the arrival of X-rays, fast ions and debris ions,

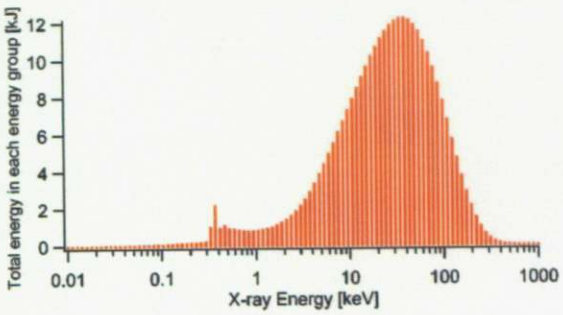

Fig. 5.2: Spectrum of X-ray from the core plasma

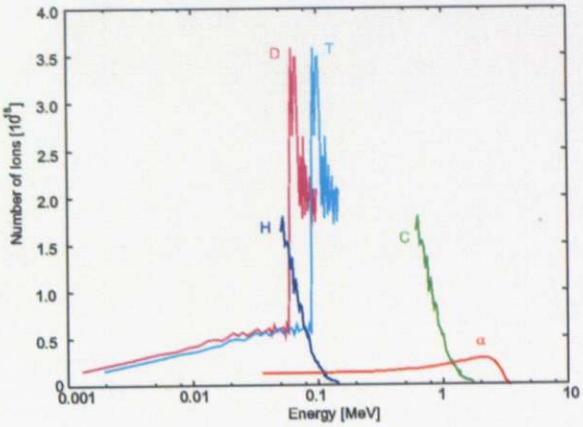

Fig. 5.3: Spectra of charged particles from the core plasma

respectively, on the surface temperature. The surface temperature reaches at its maximum ($\sim$ 1400 K) at the arrival of debris ions (around 3 μsec). The region that undergoes such rapid temperature elevation is only thin layer close to the surface. The region deeper than 50 μm only undergoes a gradual temperature increase and a quasi steady state is achieved in the region deeper than 100 μm.

Figure 5.5 shows the temperature evolution at the tungsten surface, interface between tungsten and F82H, and coolant side of F82H for 10 sec from the first shot. Here we assume 30 Hz repetition of fusion burn according to the system design described in chapter 6. As you can see, temperature of the whole region gradually increases due to the heat accumulation but it saturated and reaches some equilibrium state within 10 sec because heat flux removed by convection also increases with the increase of temperature difference between coolant and F82H. The saturated maximum surface temperature is around 1600 K. It is much lower than melting point (3680 K) and the threshold temperature of surface roughening (2400 K) which is obtained by experiments [47].

Therefore, the temperature increase in not a concern for this type dry first wall under the assumed condition (40 MJ target yield, 30 Hz repetition, chamber radius of 5.64 m). However, such a large temperature elevation may cause large thermal stress. The next subsection discusses about a thermo-mechanical analysis.

5.3 Thermomechanical analysis

5.3.1 Model description

Thermomechanical analysis was carried out by using a commercial FEM code ANSYS with the heat deposition profile analyzed in the previous subsection. Figure 5.6 shows the model used in this

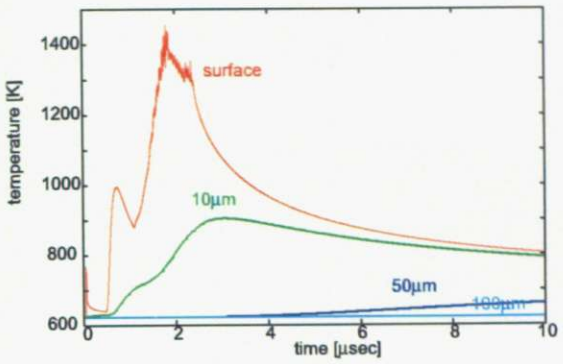

Fig. 5.4: Temporal temperature evolution at various depths of the first wall during the first shot

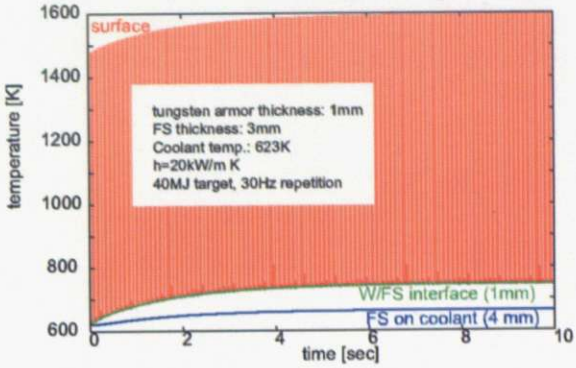

Fig. 5.5: Temporal temperature evolution of the first wall during 10 sec from the first shot

calculation. To reduce computational load, axisymmetric 2-D geometry was used. The main purpose of this study is to obtain an overall stress distribution. Then here we approximately describe an infinite plane by giving displacement coupling as the condition of constraint at the side surface (effective restrain of bending). Temperature dependant mechanical properties are obtained from reference [48]. A simple bilinear condition (see Fig. 5.7 was assumed for the relation between stress and strain of tungsten and no dynamic effect was considered.

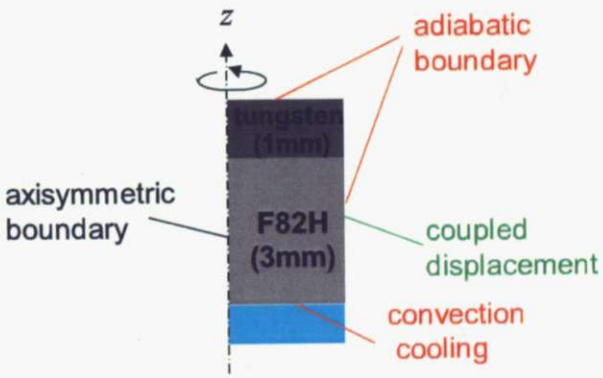

Fig. 5.6: Schematic view of the model used in the thermomechanical analysis

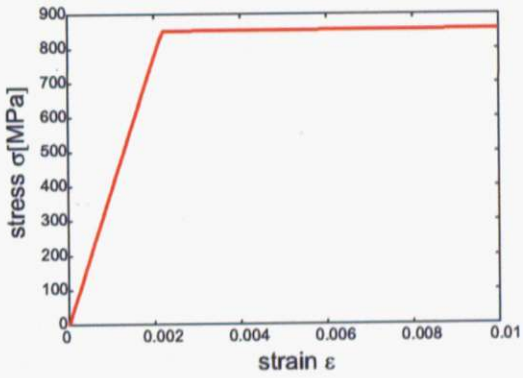

Fig. 5.7: Relation between stress and strain of tungsten used in this calculation

5.3.2 Result and discussion

Figure 5.8 shows the stress-strain behavior during the first shot. Temporal evolution of strain for the first 10 μsec is shown in Fig. 5.9. Figure 5.10 describes the contribution of each components (elastic, plastic and thermal) to total strain of the surface and their relationships between temperature.

As you can see from these figures, the region near the surface undergoes yield and plastic deformation not only in heating phase but also in cooling phase. The maximum plastic strain at the surface is about

0.01 (compression) and residual stress and strain is around 1 GPa (tensile) and 0.001 (compression), respectively. The deeper region (5 μm or more from the surface) does not undergo plastic deformation in cooling phase. The region deeper than 20 μm does not undergo any plastic deformation.

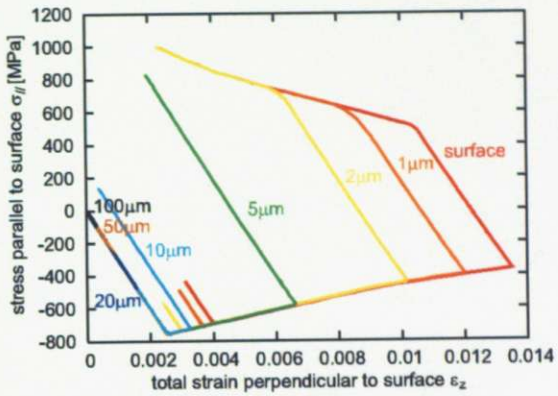

Fig. 5.8: Stress-strain behavior at various depths of the first wall during the first shot

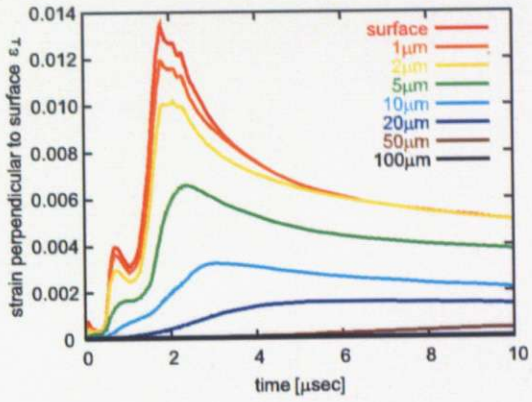

Fig. 5.9: Temporal evolution of total strain at various depths of the first wall during the first shot

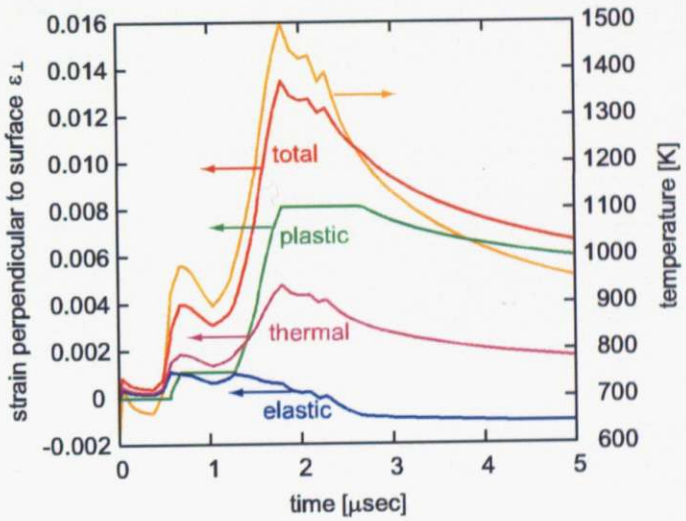

Fig. 5.10: Temporal strain evolution at the first wall surface during the first shot. Temperature evolution is also plotted (right scale).

As shown in figure 5.11, most metals shows low cycle fatigue if they undergo plastic deformation [49–51]. In this case, metals reach final rupture at the number of cycle around 10^6–10^7. Whereas the number of shots for 30 Hz repetition reaches about 10^9 per a year. Thus low cyclic failure may disable the design of a dry wall chamber.

The most simple way to solve this problem is to use a larger chamber and avoid plastic deformation.

From figure 5.10 we can see that tungsten yields and starts plastic deformation around 900 K. Figure 5.12 shows temporal temperature increase with the same condition as Fig. 5.5 except that the chamber radius is 9.2 m. It indicates that plastic deformation and low cycle fatigue failure can be avoided if the chamber radius $R > 9.2$ m. But such a large size chamber has higher construction cost and disable the cask maintenance method of blanket (see chapter 3).

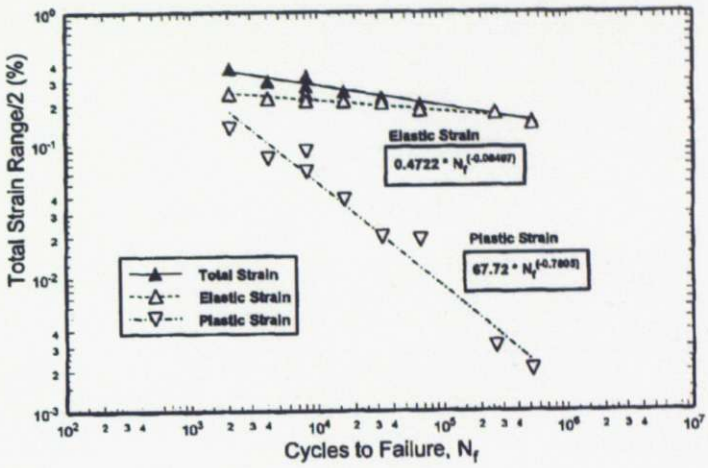

Fig. 5.11: S-N diagram of reduced activate ferritic steel F82H (Fig. 1 of reference [49])

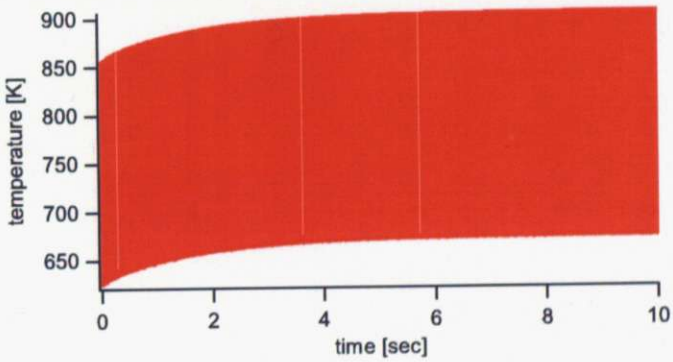

Fig. 5.12: Temporal temperature evolution of the first wall during 10 sec from the first shot in case of the chamber radius of $R = 9.2$ m

Under an IFE condition, however, strain rate is quite large. As you can see from Figs. 5.9 or 5.10, the strain reaches 0.01 within 2 μsec. Then strain rate is quite large, $\dot{\varepsilon} \sim 10^4$ /s. Under such a high strain-rate state, the mechanism of deformation is totally different from the one under a quasi-static state [52,53]. Under a quasi-static state, slipping is a dominant mechanism of deformation. But under a high strain-rate state, deformation is dominated by twinning and grain decohesion. In this case,

mechanical properties of material also changes. Figure 5.13 shows experimentally obtained stress-strain curves of 4 tungsten samples with different heat treatment. Solid line shows the data measured in quasi-static deformation ($\dot{\varepsilon} = 10^{-3}$ /s), broken line and dotted line show the data measured in high strain rate deformation ($\dot{\varepsilon} = 10^{3}$ /s and $3 - 4 \times 10^{3}$ /s, respectively). Apparently, yield strength under high strain rate increases to about twice of static deformation. Not only tungsten but also many bcc metals are known to show similar tendency [54].

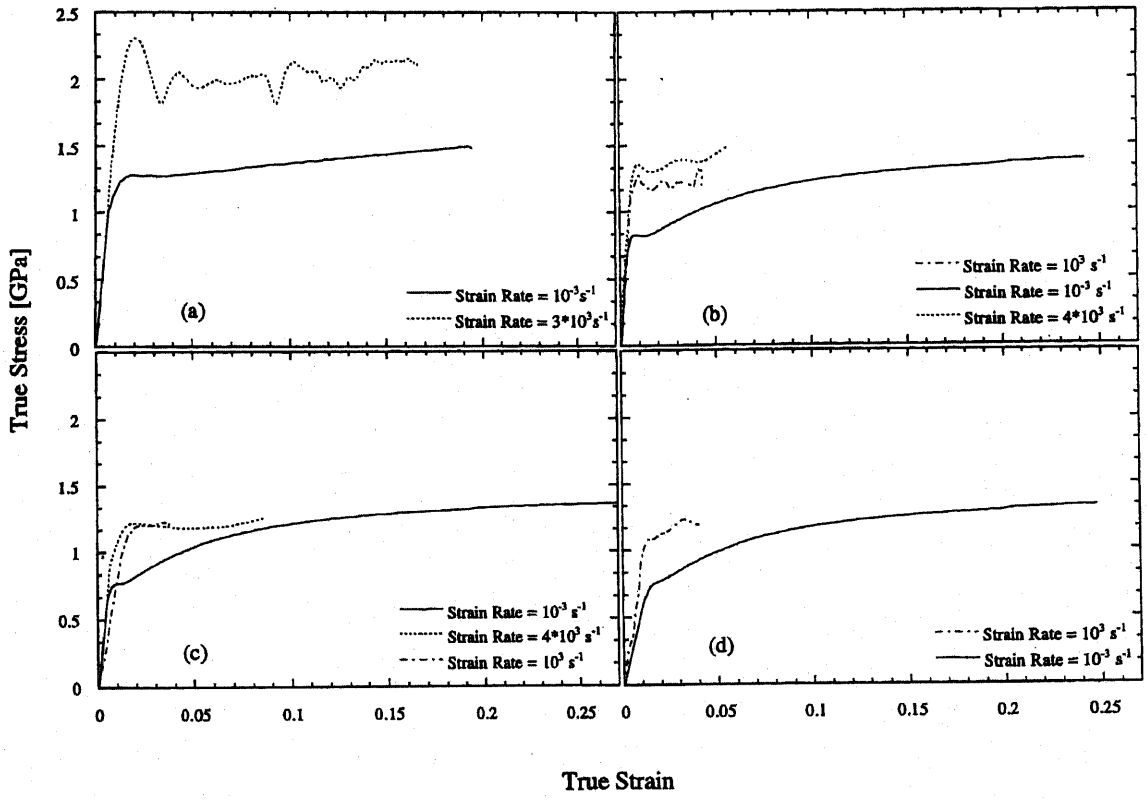

Fig. 5.13: Stress-strain curves for tungsten at different strain rates: (a) as-received; annealed (b) at 2023 K, (c) at 2873 K, and (d) at 3073 K.

Grain size also gives a great influence on the yield strength. Grain boundary decohesion stress decreases with the increase of grain size. This considered to be caused by a concentration of impurity. The grain-boundary impurity concentration c_{GB} in unit area is directly proportional to the grain-boundary area per unit volume:

$$c_{GB} = n\frac{\pi d}{3} \tag{5.2}$$

where n is the impurity content in unit volume and d is the grain size. A decrease in the grain-boundary

decohesion stress Δ_{GB} is caused by an increase in c_{GB}, which can be then described as

$$\sigma_{GB} = \sigma_{in} - \Delta_{GB}(c_{GB}) \tag{5.3}$$

where σ_{if} is the decohesion stress of a "clean boundary". It is also known that both the flow and twinning stresses, σ_y and σ_T, increase with the decrease in the grain size. They can be described by Hall-Petch relationships as a function of grain size [55]:

$$\sigma_y = \sigma_0 + \frac{k_S}{\sqrt{d}} \tag{5.4}$$

$$\sigma_T = \sigma_{0T} + \frac{k_T}{\sqrt{d}} \tag{5.5}$$

where σ_0 and σ_{0T} are the frictional stresses for slip and twinning, respectively. k_S and k_T are the Hall-Petch slope for twinning and slip, respectively, which are experimentally determined. These relationships Eqs. (5.3)–(5.5) indicates a fine-grained material can show much higher strength than as-received one. Actually, experimental result in Fig. 5.13 also indicates the increase of yield stress with the decreasing grain size, since grain size becomes larger when the sample is annealed in higher temperature.

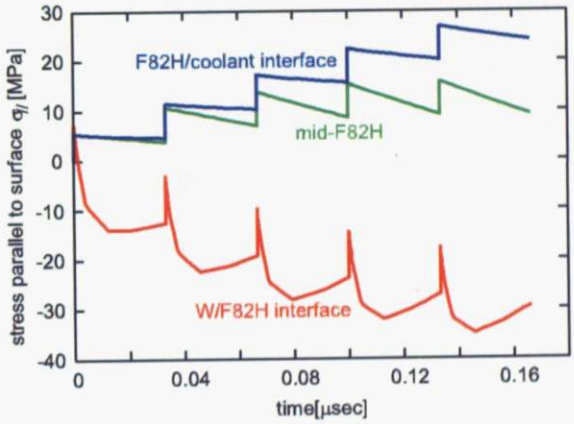

Fig. 5.14: Temporal stress evolution of F82H at the interface to tungsten, the midplane, and the interface to coolant.

In contrast, thermal stress in the structural material is not a concern. Figure 5.14 shows the temporal evolution of stress at the interface of tungsten and F82H, the midplane of F82H and the interface of F82H and coolant during the first five shots. It can be seen that the absolute value of stress at each point is below 40 MPa. Considering stress is proportional to the temperature increase, stress at each point is expected to be confined within a few hundreds MPa, which is much smaller than yield stress of F82H (600 MPa even at 500 K). Then the remaining concern is the fracture strength of the interface of tungsten and F82H. There are mainly three methods to produce tungsten armor layer on F82H:

- VPS (Vacuum plasma spray)
- HIP (Hot Isostatic Pressing)
- IR processing (High-Density-Infrared Transient Liquid Coatings) [56]

VPS is one method to form the coating by spraying coating material in powder form with a plasma jet. The material is melted and sprayed on the surface of base material and resolidified. The merit of VPS is its low cost and ability of in-situ treatment. Thus coating of a large area and arbitrary thickness on any shape, anywhere located components is possible by VPS. But the layer formed by VPS has relatively high porosity then it is concerned that the deterioration of mechanical and thermal properties of the formed layer compared with a bulk material. VPS is also inevitably associated with melting and recrystallization, the grain size of coated material cannot be controlled (it becomes problem when coating fine-grained material (e.g., ultra fine-grained tungsten described in section 5.5.2)).

By contrast, relatively dense, uniform layer can be formed by HIP and IR. HIP is the method to joint two different layers by putting high pressure ($\sim$ 1 GPa) in high temperature ($>$ 1000 K) noble gas (e.g., Argon). This method utilizes the diffusion of atoms in the different layers and enables to form strong bonding including intermediate layer. The formation of such intermediate layer is effective if the component undergoes large temperature increase because it works as a cushion to reduce a difference in thermal expansion at the interface, which is the main cause of thermal stress. In addition, this method is not accompanied by the melting of coating layer and enables to bonding the fine-structural material. But it must be done in the special equipment and has the difficulty to produce large size components.

IR processing is developed in US Oak Ridge National Laboratory (ORNL) , which produces coating layer by instantly melting the coating material with a high power plasma arc lump. The merit of this method is to produce quite uniform coating layer without generation of the intermediate layer. Thus it is favorable to produce coating in case of the intermediate material can degrade the thermomechanical properties (e.g., tungsten coating on silicon carbide (SiC), then the possible intermediate material is tungsten carbide (WC or W_2C), which is brittle and has low thermal properties), IR processing is also considered to be able to cover relatively larger area than HIP. But it using melting process and cannot control grain structure as well as VPS.

Experiments in HAPL project showed that the fracture strength of bonding between tungsten and F82H is 140–616 MPa if VPS was used to bond two materials and 450–1050 if HIP was used. Then they concluded HIP method was most reliable to produce tungsten coating on F82H [57]. Whereas another experiment held in Kyushu University [58] indicates bonding layer produced with VPS can also have

sufficient strength by optimizing the condition of VPS. Then deterioration of bonding between tungsten and F82H is not a concern in this design condition.

In addition, calculation reveals tungsten surface is kept not to be melted even if bonding is perfectly lost. Figure 5.15 shows the temporal temperature evolution of the surface of tungsten when the opposite side is cooled by only radiation heat transfer. Here we assumed the heat flux removed from the cooling side can be described as a black-body radiation;

$$\dot{q} = \sigma_{\mathrm{B}}(T^4 - T_{\mathrm{cool}}^4) \tag{5.6}$$

where T, T_{cool} are the temperature of tungsten at cooling side and coolant (assumed to be 623 K), respectively, and σ_{B} is Stefan-Boltzmann constant

$$\sigma_{\mathrm{B}} = \frac{2\pi^5 k^4}{15c^2h^3} \,. \tag{5.7}$$

This result also indicates the possibility of "detached" armor design. Although the effect caused by thermal stress becomes more severe due to the increase in temperature, this type of armor can be one alternative option because it can be easily replaced.

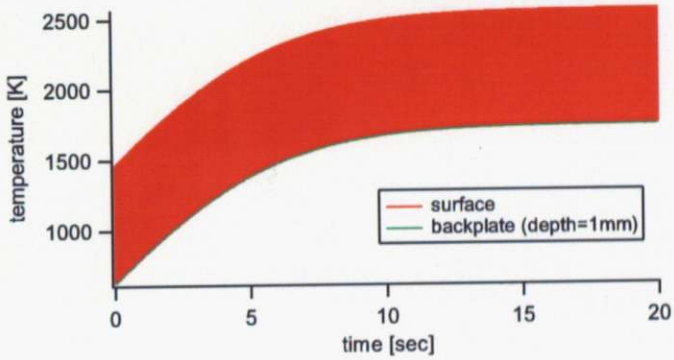

Fig. 5.15: Temporal temperature evolution of the first wall during 10 sec from the first shot in case that the first wall is only radiatively cooled

5.4 Other critical issues on a dry wall design

5.4.1 Sputtering

In the previous section, mass loss of a dry wall due to temperature increase and accompanying thermal stress were discussed. However, the first wall of an IFE reactor chamber is also irradiated by charged particles released from burning fuel. Since there is no magnetic field and no buffer gas, an IFE chamber wall is uniformly exposed to the energetic particle irradiation. Then the effects by it also need to be considered to discuss the design feasibility of a dry wall under the IFE condition.

Most direct effect caused by energetic particles is sputtering. The mechanism of sputtering can be categorized into two main parts; chemical sputtering and physical sputtering. Chemical sputtering is one of an erosion process of solid material through chemical reaction that generates gaseous products. For example, carbon is easily eroded by an irradiation of hydrogen isotopes because generated hydrocarbons have low boiling point (e.g., methane) and can easily released from the surface. Whereas physical sputtering is pure "sputtering" process of lattice atoms by a collision of external energetic particles.

In case of tungsten, chemical sputtering is negligible. Figure 5.16 show physical sputtering yield of tungsten by proton, deuteron, alpha and carbon ion, respectively. Then loss of tungsten due to physical sputtering can be estimated. Here the maximum sputtering yield of each particle is used to carry out a conservative estimation; 0.003 atom/ion for 10 keV proton, 0.007 for 10 keV deuteron, 0.04 for 10 keV alpha particle, and 0.5 for 10 keV carbon ion. Here no data for sputtering yield of triton. Then 0.01 is used because sputtering yield almost proportional to the mass of projectile ion for light ions. The flux of each particle per unit area for 1 shot are 5.85×10^{16} /m^2 for carbon and hydrogen, 1.57×10^{17} /m^2 for deuteron and triton, and 2.37×10^{16} /m^2 for alpha particle. Then using the values of sputtering yield given in the above, the number of sputtered tungsten atoms per unit area for 1 shot is 3.31×10^{16} /m^2. Considering the density of tungsten is 6.34×10^{28} /m^3, the thickness of tungsten lost due to sputtering is 0.37 mm assuming 75 % plant availability. This value is slightly overestimated because there is no carbon and alpha particle that has the energy coincides to the maximum sputtering yield, as shown by Fig. 5.3. If the sputtering yield values for the projectile energy of 1 MeV, 0.08 for carbon ions and 0.002 for alpha particles, are used, the lost thickness is estimated to be 0.085 mm.

Considering this estimation is a conservative one, the loss of tungsten armor due to physical sputtering is within the acceptable range.

5.4.2 Blistering and exfoliation

Another concern caused by energetic particles is blistering. An energetic particle has a specific range in a solid material that is determined by energy and species of the projectile ion and the elemental species of the target material. Then gas ions are concentrated at a specific depth and generate a bubble. As bubbles are growing, high internal pressure of the gas pushes up the surface and dome-like blisters are observed on the surface. This phenomenon is called as "blistering". If bubbles further grow, bubbles are connected together and the surface becomes flaky form and finally is exfoliated. Then surface layer with the thickness coincides the range of the irradiated ion can be exfoliated.

As described in the above, blistering is occurred by gas ions; hydrogen isotopes and helium. But hydrogen isotopes can easily diffuse and are desorped from the surface when the temperature is increased to

around the depth of 2 μm, which coincides its range in tungsten.

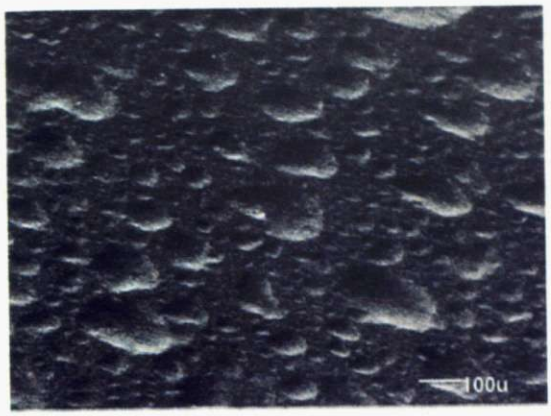

Fig. 5.17: A SEM image of tungsten test sample after irradiation of 10^{21}He/m^2 in HAPL experiment. Generation of numerous bubbles can be seen. (Fig. 2(b) from reference [61])

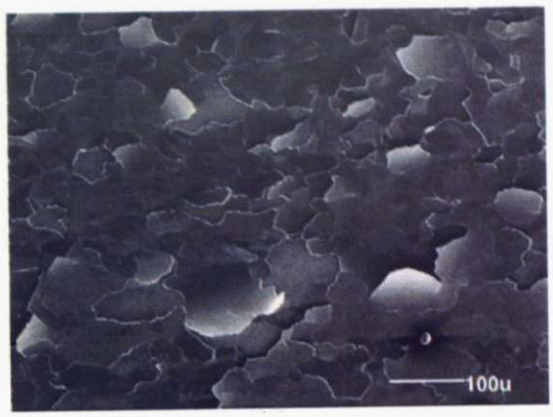

Fig. 5.18: A SEM image of tungsten test sample after irradiation of 10^{22}He/m^2 in HAPL experiment. Surface flaking and exfoliation is observed. (Fig. 2(a) from reference [61])

Whereas alpha particle energy in this design study is over the range of several tens keV to 3.5 MeV and its peak is around 2 MeV. The range of alpha particle with the energy of 3.5 MeV and 2 MeV is about 5 μm and 3 μm, respectively. In this design study, helium fluence is 3.6×10^{16}/m^2/shot in case that chamber radius is 5.64 m. The number of shots for 30 Hz repetition is about 7×10^8 per a year if assuming 75 % plant availability. Then simply assuming the layer with the thickness coincides to the range is exfoliated at the same fluence, 10^{22} He/m^2, the thickness lost in one year operation reaches 12.6 mm indeed. Such a large amount of loss cannot be acceptable. The HAPL experiment indicates that blistering occurred when helium accumulation reaches at around 4 at.% and exfoliation at 20–40 at.% (The atomic density of tungsten is 6.33×10^{22}/cm^3 and 4 at.% coincides the fluence of 5×10^{21}/m^2) . Then if assuming exfoliation is also occurred at the accumulation of 20 at.%, then threshold fluence for exfoliation is about 6.3×10^{22}/m^2 for 3.5 MeV and 3.8×10^{22}/m^2 for 2 MeV. In this case, by using threshold fluence of 3.8×10^{22}/m^2 from a conservative view, the lost thickness is estimated to be about 2.1 mm. This value is much smaller than that estimated by the fluence limit, but still is not allowable.

One possibility to avoid exfoliation is desorption of accumulated helium by a thermal activation effect. In fact the HAPL experiment also provided the data which indicates the absorption of helium from the surface. In one of the HAPL experiment, single crystal and polycrystalline tungsten test samples were implanted with 1.3 MeV ^{3}He at 1123 K to a dose of 10^{19} He/m^2 in multiple steps. Samples were heated to 2273 K between each step to reproduce conditions in a laser reactor since the first wall undergoes cycles of helium bombardment and temperature elevation. Samples were implanted and annealed in 1, 10, 100, and 1000 steps to reach a total implanted dose of 10^{19} He/m^2. Figure 5.19 shows the relation

between relative helium retention in the sample and helium dose per one cycle. As you can see when the helium dose implanted in each cycle was 10^{16} He/m^2, polycrystalline tungsten retained ~ 30 % of the implanted helium and single crystal tungsten retained only ~ 5 %.

Generally impurity migration in a metal lattice can be described as a simple diffusion equation with the diffusion coefficient of the form:

$$D = D_0 \exp\left(-\frac{E_{\rm dif}}{kT}\right) \tag{5.8}$$

where T is the temperature and D_0 is the constant depends on elemental species. For bulk tungsten

$$D_0 = 4.7 \times 10^{-7}\ [\mathrm{m}^2/\mathrm{s}]\ . \tag{5.9}$$

is obtained from the experimental study [63]. In Eq. (5.8), $E_{\rm dif}$ is the effective diffusion activation energy. This activation energy affects much on diffusion behavior. The activation energy is determined through numerous complicated physics processes (e.g., interaction of helium with defects or other impurities) and cannot be defined by a simple form. However, the existence of 4 specific activation energies for helium in tungsten has been clarified through theoretical calculation [64] (see table 5.1 and Fig. 5.20).

Here helium formation energy is the energy required to introduce a helium atom in a metal lattice. Since the metal conduction band must be shielded off from the closed electron shell of a helium atom to introduce it in a lattice, the formation energy is large. This means helium can easily migrate in the lattice and migration energy of interstitial helium is small. Then helium tends to disengage from

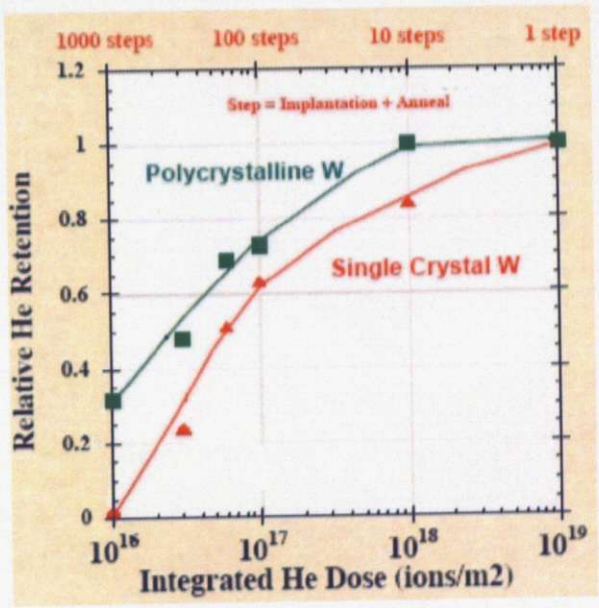

Fig. 5.19: Relative helium retention in polycrystalline and single crystal tungsten samples as a function of helium does per cycle for different number of pulses with temperature anneals (Figure 7 of reference [65].)

Table 5.1: Specific activation energies and these values of helium in a metal lattice.

Helium formation energy E^{f}_{He}:	5.47 eV
Helium migration energy E^{m}_{He}:	0.24 eV
Helium-vacancy binding energy $E^{b}_{He\text{-}V}$:	4.15 eV
Helium-vacancy dissociation energy $E^{diss}_{He\text{-}V}$:	4.39 eV

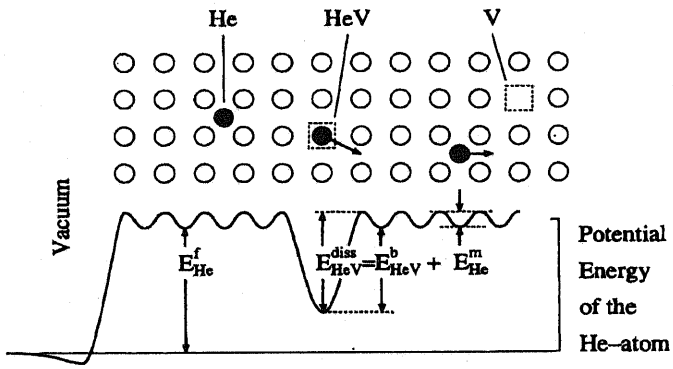

Fig. 5.20: Schematic view of the positions and corresponding energy of a helium in a metal lattice (FIG. 1 of reference [64]).

the metal atom and concentrates in the lattice defects or vacancy. This is the reason of large helium-vacancy binding energy and large energy is required to move and desorp the helium from the metal when it combines with a vacancy.

In the HAPL design study, this activation energy was estimated through the comparison of helium retention measured by the experiment with that calculated by a simple diffusion equation [65]

$$\frac{\partial C(x,\ t)}{\partial t} = D(T)\frac{\partial^2 C(x,\ t)}{\partial x^2} \tag{5.10}$$

with a boundary condition

$$\frac{\mathrm{d}C}{\mathrm{d}x}(x = 0,\ t) = 0 \tag{5.11}$$

$$C(x = \delta,\ t) = 0 \tag{5.12}$$

where C is helium concentration and δ is system size ($x = \delta$ corresponds to the surface of the first wall and the helium that reaches this point is assumed to be released quickly). The estimated activation energy is 3.6 eV for polycrystalline tungsten and 2.4 eV for single crystal tungsten. However, in this design study, the maximum surface temperature is lower (1400 K) than the case of HAPL. It is easily found from Eq. (5.8) that diffusion coefficient strongly depends temperature. Then such helium migration and desorption can hardly be expected in the case of this design.

One of the possible methods to avoid blistering is the use of highly-engineered materials. In HAPL design study, nanostructure tungsten foam [66] (Fig. 5.21) and tungsten velvet [67] (Fig. 5.22) has been proposed as a possible candidate for the armor material of a dry wall. These materials has been developed with the idea of minimizing system size (coincides δ in Eq. (5.10)) and enhancing desorption. But such porous structure has difficulty to maintain high thermal conductivity and mechanical strength. In addition, helium migration at low temperature is quite small and desorption cannot be expected even if nanometer scale structure can be fabricated. Another method to suppress blistering is to avoid helium concentration and prevent the formation of large bubble. Here fine-grained material should be remarked because it has many grain boundaries that provide a sink of vacancy. This high density of grain boundary can also enhance the diffusion of helium along it(low activation energy of single crystal tungsten in the HAPL experiment also indicates this effect). As mentioned in the previous subsection, fine-grained materials also have the possibility to show high structural strength. Thus the use of fine-grained materials is a potent option to enable the design of a dry wall chamber.

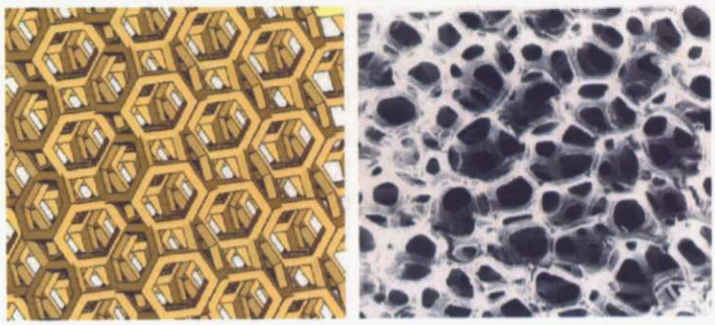

Fig. 5.21: Three dimensional solid model (left) and an optical micrographs (right) of tungsten foam (Fig. 9 from reference [66]).

5.4.3 Carbide formation

An IFE first wall is also irradiated by energetic carbon ions because carbon is contained in plastic ablator of the fuel pellet. The mobility of carbon impurity in a tungsten lattice is also very small. The diffusion of carbon in tungsten can be estimated with the diffusion coefficient as the same form of Eq. 5.8, and $D_0 = 8.91 \times 10^{-7}$ m^2/s and $E = 2.31$ eV, respectively. Then the atomic ratio of carbon to tungsten around the depth coincides to the range of carbon can soon reaches unity. According to the binary phase-diagram of tungsten and carbon [68], carbide formation is inevitable under such a carbon-rich condition. Generally metal carbide has inferior thermomechanical properties compared with pure metal. Table 5.2 shows the comparison of main thermomechanical properties of tungsten and

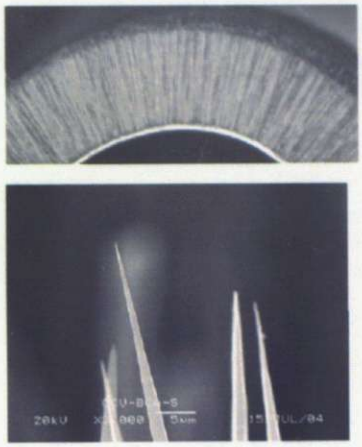

Fig. 5.22: An optical micrographs of tungsten velvet (Figure from reference [67]).

tungsten monocarbide (WC) [44]. In a steady-state operation, the effect due to carbide formation must be considered.

Table 5.2: comparison of thermal properties of tungsten and tungsten carbide

	density [g/cm^3]	melting [K] point [g/cm^3]	specific [J/kg/K] heat [J/kg/K]	thermal [W/m/K] conductivity [W/m/K]	thermal [10^{-6}/K] expansion [10^{-6}/K]
WC	15.8	2900	274[a)]	84.1	5.82-7.4
W	19.3	3683	165[a)]	182	4.5

* @1500 K

5.5 Alternative materials for a IFE dry wall

5.5.1 Required properties for the IFE dry wall

In this design study, the maximum surface temperature of a dry wall is expected to be below 2000 K. Then not only tungsten but also several materials which has melting point above 2000 K can be a candidate for the armor materials.

As discussed in the above, a lot of characteristics are required for the material used as the IFE first wall:

- high melting point
- high thermal conductivity
- high heat capacity

- low thermal expansion
- low sputtering yield
- high yield stress
- high ductility
- high mobility of impurity
- low activation
- good thermomechanical properties of carbide

In addition, from the viewpoint of the cost, high abundance is also desired.

Table 5.3 compares the properties of the bulk elements with melting point is higher than 1700 K. There is no material that meets all requirements listed in the above. From the viewpoint of thermal property, molybdenum is excellent because it has high thermal conductivity and heat capacity simultaneously. However, it can produce many activated nuclei with long half-life (e.g., ^{93}Mo : 4000 years, ^{99}Tc : 2.11×10^5 years) through fast neutron reactions. Nickel also has high thermal conductivity but produces long-life nuclei.

Table 5.3: Comparison of the properties of elements

	melting point [K]	thermal conductivity (@1400K) [W/m · K]	specific heat (@RT) [J/kg · K]	thermal expansion (@1400K) [10^{-6}/K]	sputtering yield D^+, max. [atoms/ion]	carbon diffusion E_{diff}[eV] / D_0[m^2/s]
C	3643 (sublim.)	~40	711.6	5.3	2.5×10^{-2}	7.04 / 5×10^{-4}
V	2190	42.4	485.6	13.6	1.5×10^{-2}	1.18 / 5×10^{-7}
Cr	2130	61.6	447.9	14.0	4.0×10^{-2}	1.14 / 9×10^{-7}
Fe	1809	29.9	443.7	23.3	4.0×10^{-2}	1.27 / 9×10^{-4}
Ni	1768	80.4	443.7	19.5	5.0×10^{-2}	1.47 / 1×10^{-6}
Mo	2896	99.6	2507	7.2	1.0×10^{-2}	1.77 / 5×10^{-6}
Ta	3258	61.8	139.8	7.7	5.0×10^{-3}	1.74 / 1×10^{-6}
W	3680	111	132.7	5.4	8.0×10^{-3}	2.31 / 9×10^{-7}
Pt	2042	84.8	132.7	12.3	1.5×10^{-2}	NA

Thus we selected chromium, tantalum and platinum as alternative materials for the first wall armor. Fig. 5.23 shows the temporal temperature evolution of these materials during the first shot. One can see chromium shows the thermal response very close to that of tungsten. Although thermal conductivity of chromium is only about half of that of tungsten, its high heat capacity and high heat conduction

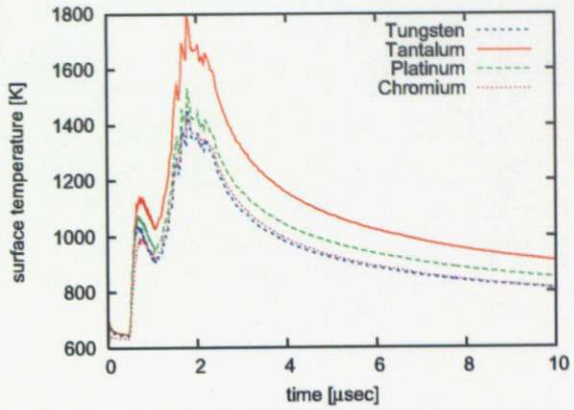

Fig. 5.23: Temporal temperature evolution of the first wall armor during the first shot if alternative materials (Cr, Ta, Pt) are used.

through the steeper temperature gradient generated by the shorter range of charged particles cancel out this defect. If chromium can be used as the first wall material, several merits are brought:

- High abundance ratio compared with raremetals like tungsten
- Thermomechanical properties close to the steel (favorable to bonding)
- Low activation
- Relatively high ductility

Whereas it also has some concerns of

- High physical sputtering yield ($\sim$ 10 times of tungsten)
- Low yield strength and high thermal expansion

Since the detailed experimental database is not available, it is not easy to evaluate the adequacy of these alternative candidates as the armor material. However, it should be remarked that the reduction of wall load by utilizing the properties of fast ignition scheme gives an impact of broadening the options of material selection.

5.5.2 Ultra fine-grained tungsten

As mentioned in preceding sections, a fine-grained material is favorable for the first wall because it has high mechanical strength and high resistivity against blistering due to helium accumulation.

Here a novel material, ultra fine-grained tungsten (UFG-W) has been developed in Tohoku University [69]. UFG-W is produced by mechanical alloying (MA) [70] of tungsten powder with a small amount

(several wt.%) of TiC powder. UFG-W has a quite fine crystalline structure (grain size is $\sim$ 50 nm, whereas as-received tungsten has 1-10 μm, see Fig. 5.24) and also shows many remarkable properties:

- high structural strength (yielding stress of twice of normal tungsten: $\sim$ 2 GPa) and high hardness
- high recrystallization temperature (more than 2000 K)
- superplasticity (achievement of 120 % plastic strain) [71]
- little irradiation hardening

The structural strength of UFG-W becomes further higher when the strain rate becomes large. Figure 5.25 shows the stress-strain curves of ECAP tungsten (tungsten of which grain size is refined to a few μm by ECAP (Equal Channel Angular Pressing) process) and UFG-W. At the strain rate of 10^4 s^{-1}, the yield stress of UFG-W can reach almost 3 GPa [72]. Then it is expected that UFG-W has no plastic deformation under condition of this design study. In addition, recent study indicates UFG-W has high resistivity against blistering. The experimental study in Tohoku University revealed that UFG-W showed almost no surface morphological change when the fluence of 3 MeV helium ion reached $10^{23}/m^2$ [73]. Unfortunately experimental data of further higher fluence is currently not available. However, this experiment indicates UFG-W has the threshold for blistering two order higher than normal tungsten.

UFG-W is very recently developed material and there is not sufficient data of its thermomechanical properties. However, past experiments indicate a large potential of UFG-W as an armor material for the component exposed to high heat and particle flux.

Since UFG-W requires HIP process for its molding, currently we can obtain only a small size (several cm diameter) sample. However it is considered that the components with at least several tens centimeters square are required for the first wall. Then the possibility of producing a large size UFG-W plate is one of the key issues. The first wall armor with UFG-W cannot be fixed by in-situ method and it must be replaced when the armor is eroded. The replacement of the first wall requires a certain time. Then the replacement needs to be carried out simultaneously with another maintenance process from the viewpoint of keeping a high plant availability. The component considered to have the shortest life-time is the final optic, of which life-time is one or two years, as discussed in chapter 3. Thus the possibility of survival for at least one year is another key issue of UFG-W armor.

5.6 Summary and proposal

According to the thermomechanical analysis and consideration on several threatening effects due to particle irradiation, it is clarified that the design of a compact dry wall chamber is not impossible, but

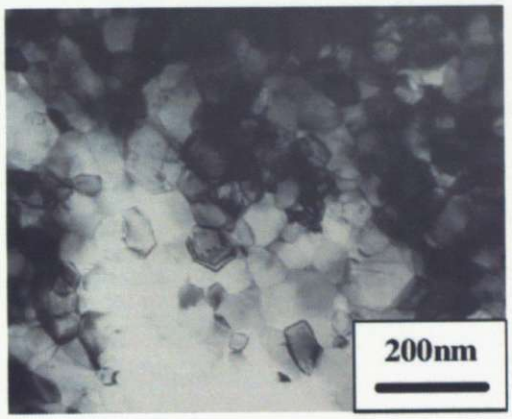

Fig. 5.24: A TEM bright-field image of the grain structure of an ultra fine-grained tungsten sample (a HIPed W-0.7%TiC compact processed with MA in an Ar atmosphere). This figure is derived from Fig. 3 of ref. [69].

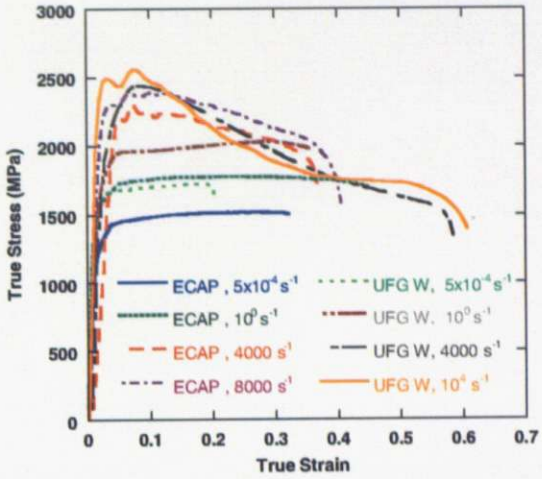

Fig. 5.25: Stress-strain curves of ECAP (Equal Channel Angular Pressing) W (grain size : a few μm) and UFG-W with different strain rates (Fig. 3 of reference [72]).

still difficult even the wall load is minimized by utilizing the fast ignition scheme. The critical issues in the dry wall design are:

- possibility of the rupture of the armor material due to low cycle fatigue
- mass loss of the armor material through blistering and surface exfoliation due to helium accumulation

Then ultra fine-grained tungsten is remarkable because of its high mechanical strength and possibility of suppression of blistering.

The reduction of wall load also gives us an option of using alternative materials. For example, alloys have relatively low melting point compared with elemental materials but it is possible to apply them a special function by adjusting the concentration of additional elements. It is required to select the optimum material by examining various properties with consideration that the material is used under a steady state, high energy particle irradiation.

Chapter 6

System Design

6.1 Development of a system design code

The purpose of this study is to design a laser fusion reactor plant for a commercial use. Then the evaluation of plant economic efficiency through cost analysis is also quite important as well as the feasibility study on physics and engineering issues. Thus we have developed a system analysis code that can estimate plant performance including cost analysis.

This system code consists of three main parts:

- calculation of fusion gain
- calculation of plant output, the condition of the chamber and the final optics
- cost analysis

The first part is the same as 0-D analysis model described in chapter 3. Thus here a brief review of the calculation model for the latter two parts is given.

6.1.1 Evaluation of plant performance

(1) Input parameters

In the design of a commercial reactor, plant economic efficiency also need to be considered. Then the design feasibility depends not only core plasma performance (i.e., fusion gain) but also plant availability, which is determined by the frequency and efficiency of the maintenance scheme. Then the load limit on the chamber wall and final optics, and the maintenance option must be considered carefully. The developed system code, however, does not consider any restriction because the purpose of this code is to clarify the possible operation regime and accompanying physics and engineering issues.

Then in this system code the following 9 parameters are initially given;

•inner radius of the reactor chamber R

•energy multiplication through neutron reaction in the blanket M

•plant thermal efficiency $\eta_{\rm th}$

•electric-optic convergence efficiency of implosion laser $\eta_{\rm Lc}$

•electric-optic convergence efficiency of heating laser $\eta_{\rm Lh}$

•recirculating power ratio (except laser) to the plant net output $f_{\rm aux}$

•repetition rate of laser irradiation $f_{\rm rep}$

•distance of the final optics from the chamber center $R_{\rm opt,c}$, $R_{\rm opt,h}$

(2) Average pulse heat load on the first wall

The average pulse heat load on the first wall for each shot $E_{\rm w}$ is given by

$$E_{\rm w} = \frac{0.2E_{\rm fus}}{4\pi R^2} \ . \tag{6.1}$$

Here considering the contribution of the energy delivered by alpha particles because neutrons can easily penetrate the first wall.

(3) neutron load on the first wall and final optics

Neutron load on the first wall and final optics is calculated with the minimum distance of them from the center of the reactor chamber.

(4) Thermal and electric output

Thermal output $P_{\rm th}$ is given by the sum of contribution of neutrons and alpha particles. Considering the energy multiplication effect through the exothermal nuclear reaction n(^{6}Li, t)α, thermal output can be written with the energy multiplication factor M as

$$P_{\rm th} = (0.8M + 0.2)\frac{f_{\rm rep}}{N_{\rm mdl}}E_{\rm fus} \ , \tag{6.2}$$

where $f_{\rm rep}$ is the repetition rate of laser irradiation. Considering the option of multi chamber systems like KOYO, repetition rate is divided by the number of reactor module $N_{\rm mdl}$.

Then plant gross electric output $P_{\rm e,g}$ is

$$P_{\rm e,g} = \eta_{\rm th}P_{\rm th}N_{\rm mdl} \tag{6.3}$$

where $\eta_{\rm th}$ is the plant thermal efficiency.

The required electric power for the laser drive is given as

$$P_{\rm L} = f_{\rm rep}\left(\frac{1}{\eta_{\rm Lc}}\frac{E_{\rm c}}{\eta_{\rm c}} + \frac{1}{\eta_{\rm Lh}}\frac{E_{\rm h}}{\eta_{\rm h}}\right) . \tag{6.4}$$

The electric power consumed by the target injector is estimated to be 1.54 MW per a unit through the detailed design study of KOYO-Fast reactor. Since the repetition rate of target injection with this system is limited to be 2 Hz, required power for target injection is

$$P_{\rm inj} = \begin{cases} 1.54\times10^6 \times \dfrac{f_{\rm rep}}{2} & f_{\rm rep}\ :\ \text{even}, \\ 1.54\times10^6 \times \dfrac{f_{\rm rep}+1}{2} & f_{\rm rep}\ :\ \text{odd}. \end{cases} \tag{6.5}$$

Since other recirculating power is considered to be proportional to the gross electric power, then net electric output is given by

$$P_{\rm e,net} = (1-f_{\rm aux})P_{\rm e,g} - P_{\rm L} - P_{\rm inj} . \tag{6.6}$$

6.1.2 Cost analysis

The cost model is refer to the one described in the paper of Dr. Kozaki [74] in Osaka University. Plant construction cost is estimated by categorizing the plant system into the following 4 groups;

- Buildings and facilities
- Chamber equipment and other plant equipments
- Turbine, electric and miscellaneous plant equipment
- Laser system

and listing up the detailed elements and applying them scaling laws of laser power or plant thermal output. Total plant construction cost can be estimated by adding the indirect cost and the interest into the direct cost. Cost of electricity (COE) is calculated from capital cost, operation and maintenance (O&E) cost and fueling cost with considering plant availability. In what follows all units of cost is unified to billion yen.

(1) Buildings and facilities

In the cost analysis of the light water reactor (LWR), generally the construction cost of buildings and facilities is estimated by the scaling law of plant thermal output $P_{\rm th}$ (electric output is used

for the turbine buildings). Then in this model the cost is also estimated by a similar model. In the case of LWR, scaling law with $P_{\rm th}^{0.5}$ is generally applied. Then it is known LWR has an advantage of scale. By contrast, the volume of the reactor building of a laser fusion plant is considered to be proportional to $P_{\rm th}^{1.5}$ because of its spherically symmetric property. Since the distance from the chamber center to the final optics is much larger than the radius or height of the vacuum vessel, it is also possible to determine the volume of the reactor building by this distance. But the constraint for the final optics has not yet been determined well. The volume of the reactor chamber also affected by the components strongly dependent on the thermal output (e.g., cooling pipe, etc.). Then the estimation with only the location of the final optics also lacks validity.

Then reference [74]estimates the cost of reactor building to be proportional to the thermal output by considering the reduction in advance of scale compared with LWR. This is a proper way to grasp the rough tendency of an uncertain object. However, the reactor building of a fusion plant is totally different from that of a fission plant because many idiosyncratic components are installed in it. The famous Generomak model, used for the cost estimation of tokamak plant in magnetic fusion, adopts different scaling law from the fission plant based on the volume of fusion island. Thus, in this code the same scaling law as the Generomak model is used with the assumption that the volume of fusion island of a magnetic fusion reactor corresponds to that of containment vessel of an IFE reactor. For other facilities except for laser building, the same scaling law as LWR (proportional to $P_{\rm th}^{0.5}$) is used. The cost of laser building is scaled to be proportional to laser energy. Then the cost of site facilities and buildings are given as the following:

•Site facilities

$$C_{\rm SF} = 7.9 \times \left(\frac{P_{\rm th}[\rm MWth]}{3420} \right)^{0.5} \tag{6.7}$$

•Reactor building

$$C_{\rm RB} = 46.9 \times \left(\frac{V_{\rm FI}}{5100[\rm m^2]} \right)^{0.67} \tag{6.8}$$

•Laser building

$$C_{\rm LB} = 7.76 \times \frac{E_{\rm L}[\rm MJ]}{4.0} \tag{6.9}$$

•Turbine plant building

$$C_{\mathrm{TPB}} = 3.83 \times \left(\frac{P_{\mathrm{e,g}}[\mathrm{MWe}]}{1100} \right)^{0.5} \tag{6.10}$$

•Other building and facilities

$$C_{\mathrm{OB}} = 3.0 \times \left(\frac{P_{\mathrm{th}}[\mathrm{MWth}]}{3420} \right)^{0.5} \tag{6.11}$$

(2) Chamber and plant equipment

(2-1) Reactor equipment

Reactor equipment is categorized into the first wall, blanket, shielding and cavity vessel.

•First wall & blanket

The construction cost of the first wall C_{FW} is calculated with mass unit cost of the first wall material $C_{\mathrm{FW,UM}}$, the density of the first wall material ρ_{FW} and the volume of the first wall V_{FW} as

$$C_{\mathrm{FW}} = C_{\mathrm{FW,UM}} \rho_{\mathrm{FW}} V_{\mathrm{FW}} f_{\mathrm{OSC}} f_{\mathrm{Ovh}} \ , \tag{6.12}$$

where f_{OSC}, f_{Ovh} are on-site construction cost ratio and overhead cost ratio. Here both ratios are fixed to be 1.15.

Similarly, the construction cost of blanket C_{Blk} is estimated from the mass unit cost of blanket material $C_{\mathrm{Blk,UM}}$, the density of blanket material ρ_{Blk} and the volume of blanket V_{Blk} as

$$C_{\mathrm{Blk}} = C_{\mathrm{Blk,UM}} \rho_{\mathrm{Blk}} V_{\mathrm{Blk}} f_{\mathrm{C}} \tag{6.13}$$

where f_{C} is cost ratio and fixed to be 1.32.

•Cavity vessel & shield

The construction cost of cavity vessel C_{CV} is estimate from the mass unit cost of cavity vessel $C_{\mathrm{CV,UM}}$, the density of cavity vessel material and ρ_{CV} the volume of cavity vessel V_{CV} as

$$C_{\mathrm{CV}} = C_{\mathrm{CV,UM}} \rho_{\mathrm{CV}} V_{\mathrm{CV}} f_{\mathrm{OSC}} f_{\mathrm{Ovh}} \ . \tag{6.14}$$

The construction cost of shielding (C_{Sld}) is also calculated from the mass unit cost of shielding material $C_{\mathrm{Sld,UM}}$, the density of shielding material ρ_{Sld} and the volume of shielding material V_{Sld} as

$$C_{\mathrm{Sld}} = C_{\mathrm{Sld,UM}} \rho_{\mathrm{Sld}} V_{\mathrm{Sld}} f_{\mathrm{C}} \ . \tag{6.15}$$

The construction cost of containment vessel C_{SV} is estimated to be 25% of the sum of the cost of cavity vessel and shiedling.

(2-2) Other plant equipment

The cost of other plant equipments (reactor cooling system, tritium recovering system, etc.) except for target injection system is estimated by the scaling law of plant thermal output. In the estimation of the cost of target injection system, the number of system is also considered as in the estimation of energy consumption in Eq. (6.5).

•Heat transport system

$$C_{\mathrm{HTS}} = 40 \times \left(\frac{P_{\mathrm{th}}[\mathrm{MWth}]}{2450 \times N_{\mathrm{mdl}}} \right)^{0.7} \times N_{\mathrm{mdl}} \tag{6.16}$$

•Tritium recovery system

$$C_{\mathrm{TRS}} = 6.0 \times \frac{P_{\mathrm{th}}[\mathrm{MWth}]}{3300} \tag{6.17}$$

•Target injection system

$$C_{\mathrm{TIS}} = \begin{cases} 4.0 \times \dfrac{f_{\mathrm{rep}}}{2} & f_{\mathrm{rep}} : \text{even} \\ 4.0 \times \dfrac{f_{\mathrm{rep}}+1}{2} & f_{\mathrm{rep}} : \text{odd} \end{cases} \tag{6.18}$$

•Radioactive waste treatment system

$$C_{\mathrm{RWS}} = 10 \times \left(\frac{P_{\mathrm{th}}[\mathrm{MWth}]}{3300} \right)^{0.67} \tag{6.19}$$

•ventilation and air controlling system

$$C_{\mathrm{ACS}} = 20.1 \times \left(\frac{P_{\mathrm{th}}[\mathrm{MWth}]}{7920} \right)^{0.5} \tag{6.20}$$

•Maintenance equipment

$$C_{\mathrm{ME}} = 12.2 \times \left(\frac{P_{\mathrm{th}}[\mathrm{MWth}]}{7920} \right)^{0.5} \tag{6.21}$$

•Other reactor plant equipment

$$C_{\mathrm{OPE}} = 6.8 \times \left(\frac{P_{\mathrm{th}}[\mathrm{MWth}]}{3420} \right)^{0.5} \tag{6.22}$$

(3) Turbine, electric and miscellaneous plant equipment

(3-1) Turbine and electric plant equipment

The construction cost of turbine plant and electric plant equipments are estimated by the scaling law of plant electric power based on the actual performance of LWR.

•Turbine plant equipment

$$C_{\mathrm{TPE}} = 60 \times \left(\frac{P_{\mathrm{e}}[\mathrm{MWe}]}{1100 \times N_{\mathrm{mdl}}} \right)^{0.8} \times N_{\mathrm{mdl}} \tag{6.23}$$

•Electric plant equipment

$$C_{\mathrm{EPE}} = 35 \times \left(\frac{P_{\mathrm{e}}[\mathrm{MWe}]}{1100} \right)^{0.4} \tag{6.24}$$

(3-2) Miscellaneous plant equipment

The cost of miscellaneous plant equipment is estimated by multiplying the cost ratio of miscellaneous plant equipment f_{MPE} to the sum of the cost of building, facilities and each plant equipments calculated in the above and the cost of laser system described in the following. Although the cost ratio of miscellaneous plant equipment cannot be determined unless the detailed design is carried out, the actual performance in LWR is 3 %.

(4) Laser system

The cost of laser system is categorized into laser optics, laser diode and other laser equipment and calculated by adding engineering cost and construction cost into them.

There are a lot of uncertainties in the cost estimation of the heating laser. In reference to the detailed cost estimation of KOYO-Fast reactor design, the total cost of laser components per unit energy for heating laser is 1.4 times higher than that of implosion laser [7]. Then it is assumed that the same scaling law as implosion laser can be available for heating laser and the cost per unit power is 1.4 times larger than implosion laser.

(4-1) Laser optics

The cost of laser optics consists of the cost of laser material (e.g., glass for glass laser), laser controlling system and laser cooling system. Each cost is estimated by the scaling law of

laser energy or laser power with the cost of laser glass per unit energy $C_{\mathrm{LG,E}}$ [kyen/J].

•Laser glasses

$$C_{\mathrm{LG}} = C_{\mathrm{LG,E}} \times (E_{\mathrm{Lc}}[\mathrm{MJ}] + 2 \times E_{\mathrm{Lh}}[\mathrm{MJ}]) \tag{6.25}$$

•Laser controlling system

$$C_{\mathrm{LCnt}} = 0.022 \times (\eta_{\mathrm{Lc}} P_{\mathrm{Lc}}[\mathrm{MWe}] + \eta_{\mathrm{Lh}} P_{\mathrm{Lh}}[\mathrm{MWe}]) \tag{6.26}$$

•Cooling system

$$C_{\mathrm{LCl}} = 0.022 \times \left\{ \left(\eta_{\mathrm{LD,c,R}} - \frac{\eta_{\mathrm{Lc}}}{\eta_{\mathrm{Lc,Tr}}} \right) P_{\mathrm{Lc}}[\mathrm{MWe}] + \left(\eta_{\mathrm{LD,h,R}} - \frac{\eta_{\mathrm{Lh}}}{\eta_{\mathrm{Lh,Tr}}} \right) P_{\mathrm{Lh}}[\mathrm{MWe}] \right\} \tag{6.27}$$

Here η_{L} is the laser efficiency. In case of implosion laser, it is the products of excitation efficiency of amplifier $\eta_{\mathrm{L,Ex}}$, optic-optic conversion efficiency $\eta_{\mathrm{L,OT}}$, wavelength conversion efficiency $\eta_{\mathrm{L,WT}}$ and transmission efficiency $\eta_{\mathrm{L,Tr}}$. Currently $\eta_{\mathrm{L,Ex}} = 0.70$, $\eta_{\mathrm{L,OT}} = 0.30$, $\eta_{\mathrm{L,WT}} = 0.70$ and $\eta_{\mathrm{L,Tr}} = 0.90$ have been achieved. Then laser efficiency is estimated to be 0.11.

For heating laser, pulse compression efficiency $\eta_{\mathrm{L,PC}}$ and efficiency of chirped pulse amplification (CPA) $\eta_{\mathrm{L,CPA}}$ are also multiplied to the above products of efficiencies. Currently $\eta_{\mathrm{L,Ex}} = 0.60$, $\eta_{\mathrm{L,OT}} = 0.30$, $\eta_{\mathrm{L,WT}} = 0.80$, $\eta_{\mathrm{L,PC}} = 0.81$, $\eta_{\mathrm{L,CPA}} = 0.40$ and $\eta_{\mathrm{L,Tr}} = 0.90$ is achieved and laser efficiency is estimated to be 0.42.

Since here DPSSL (diode pumped solid state laser) is assumed, excitation efficiency of amplifier is the product of radiation efficiency of laser diode (LD) $\eta_{\mathrm{LD,R}}$ and final accumulation efficiency of LD light after numerous quantum processes. Radiation efficiency is expected to be 70% for implosion laser and 60% for heating laser.

(4-2) Laser diode systems

The cost of laser diode consists of LD components, LD cooling system and power supply and other system. The required number of LD is proportional to its peak output. The peak output of LD is calculated by the following way.

The required LD output to obtain 1 J blue right is estimated to be $1/(\eta_{\mathrm{L}}/\eta_{\mathrm{LD,R}})$ J. Since the pulse width of exciting light is required to be about 1/2 of fluorescence lifetime τ_{LD} to

increase the accumulation efficiency, required LD peak output $P_{\rm LD}$ is given by

$$P_{\rm LD} = \frac{1}{(\eta_{\rm L}/\eta_{\rm LD,R})}\frac{1}{\tau_{\rm LD}/2} = \frac{2\eta_{\rm LD,R}}{\eta_{\rm L}\tau_{\rm LD}} \ . \tag{6.28}$$

The cost of LD cooling system is estimated to be \$0.1 per unit power of heat removal. Here required amount of heat removal is equal to be 40 % of LD input power. The cost of LD power supply, LD modularizing and LD controlling system is estimated to be \$0.3 per unit LD input power. Then the cost of each component can be estimated by the scaling law of laser energy or power with the cost of laser diode per unit power $C_{\rm LD,P}$ [yen/W] as the following:

•Laser diode components

$$C_{\rm LDCmp} = C_{\rm LD,P} \times \left(\frac{2\eta_{\rm LD,c,R}}{\eta_{\rm Lc}\tau_{\rm LD,c}[\rm msec]} \times E_{\rm Lc}[\rm MJ] + 2 \times \frac{2\eta_{\rm LD,h,R}}{\eta_{\rm Lh}\tau_{\rm LD,h}[\rm msec]} \times E_{\rm Lh}[\rm MJ] \right) \tag{6.29}$$

•LD cooling system

$$C_{\rm LDCl} = 0.011 \times 0.4 \times (P_{\rm Lc}[\rm MWe] + P_{\rm Lh}[\rm MWe]) \tag{6.30}$$

•LD power supply & other systems

$$C_{\rm LDO} = 0.033 \times (P_{\rm Lc}[\rm MWe] + P_{\rm Lh}[\rm MWe]) \tag{6.31}$$

(4-3) Other laser equipments

Other laser equipments are power supply and cooling tower. The costs of them are estimated to be 0.25/W and 0.12/W respectively, per unit laser input power. Then this cost $C_{\rm OLE}$ is given by

$$C_{\rm OLE} = 0.037 \times P_{\rm L}[\rm MWe] \ . \tag{6.32}$$

(4-4) Engineering and construction service

The cost of laser system is obtained to add the indirect cost (on-site construction cost and overhead cost) to the sum of the above estimated costs. The on-site construction cost and overhead cost are estimated to be 10 % of the direct cost.

(5) Total plant capital cost

Total plant capital cost $C_{\rm PCC}$ is calculated as the sum of the following three costs.

(5-1) Total direct & engineering cost

Total direct cost is the sum of the direct cost and the indirect cost estimated in the calculation of each element.

(5-2) Owner's costs

Owner's cost C_{Own} is the indirect cost of the employer and estimated by multiplying owner's cost ratio f_{Own} to the direct construction cost. Owner's cost ratio of LWR is 510 % and here 10 % is assumed.

(5-3) Interest during construction

Generally interest during construction r_{int} of LWR is 12.6% (based on the assumption of construction schedule: 5.5 year, annual interest: 5 %, and single payment at the middle of the construction schedule). Here the same value is used.

(6) Cost of Electricity

Cost of Electricity (COE) is obtained by dividing the sum of annual capital cost C_{C}, annual operation and maintenance cost C_{OM}, and annual fueling cost C_{F} by annual production of electricity:

$$\mathrm{COE} = \frac{C_{\mathrm{C}} + C_{\mathrm{OM}} + C_{\mathrm{F}}}{24 \times 365 \times P_{\mathrm{e,n}} f_{\mathrm{av}}} \tag{6.33}$$

where f_{av} is the plant availability.

(6-1) Annual capital cost

Annual capital cost is obtained to multiply fixed cost ratio f_{FCR} to the total plant capital cost C_{PCC}. The fixed cost ratio is calculated from remaining value ratio a, annual interest r and capital recovery factor (CRF) C_{CRF} as

$$f_{\mathrm{FCR}} = (1-a)C_{\mathrm{CRF}} + ra\ . \tag{6.34}$$

CRF for n years depreciation is given by

$$C_{\mathrm{CRF}} = \frac{r(1+r)^n}{(1+r)^n - 1}\ . \tag{6.35}$$

Then annual capital cost is given by

$$C_{\mathrm{C}} = \left\{ (1-a)\frac{r(1+r)^n}{(1+r)^n - 1} + ra \right\} C_{\mathrm{PCC}}\ . \tag{6.36}$$

Generally remaining value ratio is estimated to be 10 % including land cost.

(6-2) Annual operation and maintenance cost

Operation and maintenance cost consists of direct cost (narrowly-defined operation and maintenance cost; the sum of employment cost, repair cost, insurance cost and other annual overhead cost) and related cost (business tax, etc.) and both of them are obtained approximately by multiplying constant ratio to the construction cost. In the case of LWR, it is obtained by multiplying 34 % cost ratio to the construction cost. Here operation and maintenance cost is obtained by assuming the same cost ratio but additionally summed the replacement cost of specific components related to a laser fusion reactor.

The key components need to be consider in the calculation of replacement cost are the chamber first wall, blanket and optical apparatus in the laser system that need to be replaced at a constant period.

In the design study of KOYO reactor, it is assumed that the replacement of the first wall and blanket is carried out at every two years and the entire first wall and the portion of blanket close to the first wall (20 % of the total) are replaced. Then 50 % cost of the corresponding components is accounted for the annual replacement cost. Whereas in this design the use of the solid breeder blanket is also considered. Then it is assumed that the whole blanket system except for liquid breeder is replaced when the neutron fluence on the first wall reaches 10 MWa/m^2. Then the corresponding costs of replaced materials are account for the maintenance cost. For the laser system, it is assumed that 25 % of total components is replaced annually if the neutron fluence is the same as KOYO-Fast reactor ($F_{\mathrm{n,c}}^{\text{KOYO-Fast}} = 0.13$ MWa/m^2, $F_{\mathrm{n,h}}^{\text{KOYO-Fast}} = 0.057$ MWa/m^2) and consider the variation of replacement frequency corresponding to the actual fluence F_{n}.

Then annual operation and maintenance cost is calculated as

$$C_{\mathrm{OM}} = 0.03C_{\mathrm{PCC}} + 0.1C_{\mathrm{FW}}\left(\frac{P_{\mathrm{th}}[\mathrm{MW}]}{7920}\right) + 0.25\left(C_{\mathrm{LG}} + C_{\mathrm{LCnt}} + C_{\mathrm{LCl}}\right)\left(\frac{F_{\mathrm{n}}}{F_{\mathrm{n}}^{\text{KOYO-Fast}}}\right). \tag{6.37}$$

(6-3) Annual fueling cost

The fueling cost of laser fusion reactor is determined from the cost of deuterium and pellet manufacturing cost C_{pel}. The manufacturing cost of one pellet is expected to be 5–20 yen. In case of KOYO reactor design, construction cost of pellet factory is not considered and pellet manufacturing cost is assumed to be 16 yen including the cost of tritium recovery system. In such case fueling cost is independent of pellet size and proportional to repetition rate.

However, the most part of the pellet manufacturing cost is considered to be the construction cost of pellet factory. Of course larger area and more equipment are required to produce more pellets, but cost increase due to this effect is expected to be not so large. Then here we assume the construction cost of pellet factory to be 50 Byen from the cost analysis of the fueling cost in KOYO-Fast reactor design study. This pellet factory construction cost is included in the capital cost. Then the costs of deuterium and initially installed tritium are considered in the calculation of annual fueling cost.

6.2 Plant system design

6.2.1 Possible repetition rate

According to the study described in preceding chapters, it is clarified that :

- core plasma design of which target yield is 40 MJ with fusion gain of 100 is probable.
- dry chamber with 5.64 m radius is possible if an ultra fine-grained material is used for the first wall.

Then before finalized the design, we must consider the possible repetition rate.

From the viewpoint of plant economic efficiency, repetition rate is desired to be maximize. It is considered that the repetition rate is limited by the following three factors:

- Laser engineering technology
- Chamber vacuum pumping
- Pellet injection

For the first factor, technologically $>$ 50 Hz repetition is achievable. And 16 Hz laser system is adopted in the KOYO-Fast reactor design study. Then at least 32 Hz repetition can be achieved by using two units of this system. For the second factor, allowable chamber pressure for laser irradiation and pellet injection is 1 Pa. The number of particles in the fuel pellet of this design is 1.3×10^{20} for deuterium and tritium particles, 4.6×10^{19} for carbon and hydrogen particles. Then total number of particles is expected to be 1.6×10^{20} if assuming burn fraction as 0.2. Assuming all particle becomes gas with the temperature of 1000 K from the conservative view, evacuation requirement at a steady state is

$$(1.6 \times 10^{20}) \times (1.38 \times 10^{-23}) \times 1000 \times 30 = 66 \ [\mathrm{Pa \cdot m^3/s}] \ .$$

This value is 7 times larger than the estimation in the design study of KOYO-Fast.

However, as shown in chapter 3, blanket and vacuum boundary is separated in this design to enable the simple maintenance scheme. Then the above evacuation requirement only needs to be met in the entire reactor room and it can be sufficiently achieved considering the size of reactor room. Thus the remaining problem is whether sufficient conductance from the inside blanket to the reactor room can be obtained.

The conductance of the tube with radius D and length L can be calculated with the formula of molecular flow as

$$C[\mathrm{m}^3/\mathrm{s}] = \frac{1}{6}\sqrt{\frac{2\pi RT}{M}}\frac{D^3}{L} = 38.1\left(\frac{T}{M}\right)^{0.5}\frac{D^3}{L} \tag{6.38}$$

where M and T are the molecular weight and temperature of the gas and the unit of D and L in meter and T in Kelvin.

In this design $L = 1$ m and $D = 20$ cm is assumed for the port of implosion laser. Then one beam port has the conductance of 1.80 m^3/s. Since we use total 31 beams for implosion, total conductance becomes 55.7 m^3/s. In addition, beam port of fast ignition laser can also be used as a pumping port. The conductance of it is expected to be 28.1 m^3/s if assuming $D = 50$ cm. Considering this assessment is quite conservative, it is sufficient to evacuate gas from the operation with 30 Hz repetition.

For the last factor, the use of multiple injectors remove the technological limit on the repetition of pellet injection. However, pellet injection speed is around 500 m/s and chamber size is around 10 m. Since pellet injection in the chamber before the irradiation of the preceding pellet is not allowed, the maximum repetition rate is limited to be around 50 Hz.

According to these considerations, we adopted repetition rate of 30 Hz for the reference value of this design study.

6.2.2 Other issues in the system design

Effect of the tungsten dust

As described in section 5.4.2, the loss of tungsten due to exfoliation is inevitable in this design. The total amount of exfoliated tungsten when UFG-W is used for the first wall is totally unknown. Then from the conservative view, here we assume the full of 1 mm-thickness layer is lost in a year. Then the total mass of the exfoliated tungsten is $4\pi \times 5.64^2 \times 0.001 \times 19250 = 770$ kg/year. The exfoliated tungsten is expected to have the thickness of blister cap and the size close to the helium bubble. For simplicity, assuming all tungsten dusts has 20 μm radius and 3 μm thickness. Then the average mass of the tungsten dust is 7.23×10^{-11} kg and the total number of the dusts generated in a year is estimated to be 1.06×10^{13}. Suppose that the amount of accumulated dusts in the chamber reaches a steady state

in a steady state operation. Then let τ is residence time of the tungsten dust, the density of tungsten dusts in the chamber is estimated to be $4.47 \times 10^2 \tau$ /m^3.

The problem is whether these dusts affect the implosion. If the dust with the size estimated in the above collides with a compressed pellet, it can perfectly cover the pellet and hinder the fast ignition. The implosion also can be interrupted if sufficient amount of dusts exist in the beam path and scatter the laser energy. First we consider the former issue. The volume of compressed pellet with 40 μ m diameter is 2.68×10^{-13} m^3. Then the number of dusts in this volume is estimated to be $1.20 \times 10^{-10} \tau$. This number have no significant impact unless τ exceeds 10^7 sec $\sim$ 115 day. Though there are a lot of uncertainties in the residence time of the tungsten dust, it is expected to be about a day. Thus hinder of fast ignition due to the tungsten dust is not a concern.

To consider the latter problem, first we estimate the volume included in the beam path. The diameter of beam on the final optics (located 20 m from the chamber center) is 20 cm. By approximating the shape of focused beam as a cone for simplicity, the diameter of beam at the chamber inner wall is 5.6 cm. Then the volume included in the one beam path is 4.60×10^{-3} m^3. Next we estimate the effective area covered by tungsten dusts at the location x [m] from the chamber center S. Let n, s are the density and surface area of tungsten dust exists in the point and considering the beam diameter at the point is $x/100$, S is given by

$$S = ns\frac{\pi}{4}\left(\frac{x}{100}\right)^2 . \tag{6.39}$$

Here $n = 4.47 \times 10^2 \tau$ /m^3. Assuming all tungsten dusts point the direction perpendicular to the beam path from conservative view, $s = \pi(1.0 \times 10^{-5})^2 = 3.14 \times 10^{-10}$ m^2. Whereas the beam intensity at distance x m from the chamber core is estimated to be $(R/x)^2$ times larger than that at the inner chamber wall; $x = R = 5.64$ m. Then energy flux lost due to the tungsten dusts is

$$ns\frac{\pi}{4}\left(\frac{x}{100}\right)^2\left(\frac{5.64}{x}\right)^2 E = ns\frac{\pi}{4}\left(\frac{5.64}{100}\right)^2 E \tag{6.40}$$

where E is the energy flux at the inner chamber wall. Finally we obtain the energy loss by the tungsten dust;

$$\begin{aligned}\int_0^{5.64} ns\frac{\pi}{4}\left(\frac{5.64}{100}\right)^2 E dx &= (4.47 \times 10^2 \tau) \times (3.14 \times 10^{-10}) \times 10^{-4} \times 5.64^2 \times E \times 5.64 \\ &= 1.95 \times 10^{-9} \tau E \end{aligned} \tag{6.41}$$

It is considered that more than 0.5 % of beam energy is lost, the implosion can be affected. The residence time of tungsten that can cause such loss is $\tau = 2.5 \times 10^6$ sec $\sim$ 30 day. Thus the latter problem also is not a concern.

According to these considerations, it is considered that steady state operation with a tungsten dry wall is feasible if the dust is generated and stay for a day in the reactor chamber.

Pellet injection and heating without cone guide

As described in section 6.2.1, we considered 30 Hz repetition to achieve moderate output with the small target yield. The high repetition of pellet injection is achievable by using multiple injectors. But in this case, the direction of the injected pellet differs by the location of the injector. Then fast ignition with cone guide becomes impossible because it is difficult to direct the cone to the heating laser if the pellet is injected from the oblique direction to the beam path of the heating laser.

Then two problems arise. One is the feasibility of fast ignition without cone guide. About this issue, several experimental studies have been carried out and demonstrated the principle of its physics mechanism [75]. But efficient coupling from heating laser to the compressed core as obtained with cone guide has not yet achieved. The cone guide not only helps the focusing but also contributes to efficient production of the fast electron. Then it is expected that much efforts are needed to achieve efficient heating without cone guide. The other is the tracking of the target. The pellet without cone is quite light. Especially, in this design the pellet is small to suppress its target yield and the mass of pellet is only 0.6 mg. Then target tracking may become very difficult. The idea of correcting target orbit by using magnetic lens has been proposed by the research group in Utsunomiya University [76]. However correction of the location of the pellet after injection into the chamber is still quite difficult.

Since it is difficult to evaluate the feasibility of these issues without the experimental approach, we skip the further discussion. But these problems must be considered at the phase of the detailed design.

6.3 Designed plant parameter

The basic design parameters of this design study are listed in Table 6.1. Tables 6.2 and 6.3 show the result of cost analysis by using the developed system design code. The circle chart of cost breakdown and the stacked bar chart of COE are also shown in Figs. 6.1 and 6.2. In the calculation of COE, $C_{\mathrm{CRF}} = 10.97$ % is adopted by assuming 8 % annual interest and 16 years of depreciation.

Here we select the design point with the laser energy of 400 kJ, which is estimated by 0-D model and demonstrated by 1-D hydrodynamic simulation. The radius of chamber is selected to be 5.64 m according to the thermomechanical analysis. By increasing the repetition rate up to 30 Hz, net electric output becomes to be about 400 MWe, comparable to a medium scale plant.

The point should be remarked is the low cost ratio of the laser system. Since the cost of laser system is almost proportional to its energy, this design, with relatively small laser energy, has quite small ratio

($\sim$ 10 %) of the laser system cost to the total. The cost of laser system varies greatly by the assumed unit cost of the laser glass and the laser diode (LD). In this cost analysis, the cost of laser glass per unit energy is assumed to be \$100/J. And the cost of LD per unit power is expected to be reduced to \$0.01 /W due to the improvement in the technical proficiency and the effect of manufacturing economy of scale. Especially, the influence of LD cost in the total cost is quite large. The total cost can be increases twice of the original value if assuming unit cost of LD to be 10 times higher. Then the low cost ratio of the laser system can be another merit of this design.

One can see the cost of electricity (COE) of this design is much higher than that of a existing commercial plant. Of course it is unclear whether the current COE value will be kept in the future, but it is the COE of this design is still high. This high COE is caused by the high construction cost. The total capital cost of this plant is smaller than that expected in the design study of other fusion commercial plants because of the small chamber size. However, it is still higher than a nuclear fission plant or a fossil fuel plant (200–300 Byen). Whereas the electric output of this design is less than half of such commercial plants ($\sim$ 1 GWe). Then COE becomes much higher. This is one of the issues to design a commercial laser fusion plant with a dry wall chamber. However, especially in the introduction phase, it is important to reduce the construction cost of a plant. In addition, a laser fusion plant can easily vary its output by adjusting the repetition rate. This flexibility in the operation as well as the low construction cost may help the introduction of this plant.

Table 6.1: Basic parameter of the designed laser fusion plant

chamber radius R [m]	5.64
coupling efficiency of implosion laser η_c	0.05
coupling efficiency of heating laser η_h	0.2
injection energy $E_{\rm in}$ [MJ] (implosion/heating)	0.4 (0.35/0.05)
fusion gain G	101
target yield $E_{\rm fus}$[MJ]	40
pulse heat load (except for neutrons) [J/cm^2]	2.0
repetition rate $f_{\rm rep}$ [Hz]	30
neutron wall load [MW/m^2]	2.4
energy multiplication in blanket M	1.2
plant thermal output $P_{\rm th}$ [MWth]	1385
gross electric power $P_{e,\rm g}$ [MWe]	575
recirculation power for laser drive $P_{\rm L}$ [MW]	154
net electric power P_e [MWe]	369

Table 6.2: cost parameter of the designed plant (unit : Byen)

building and facilities	55.4
first wall, blanket, vacuum vessel	60.1
turbine and electric plant equipment	62.7
heat transport system	26.8
target factory and target injection system	55.0
other plant equipment (ventilation etc.)	36.4
laser system	33.5
direct construction cost	330.0
total plant capital cost	404.6

Table 6.3: cost of electricity of the designed plant (unit : yen/kWh)

capital	18.31
operation and maintenance	10.92
fueling	0.28
cost of electricity (COE)	29.51

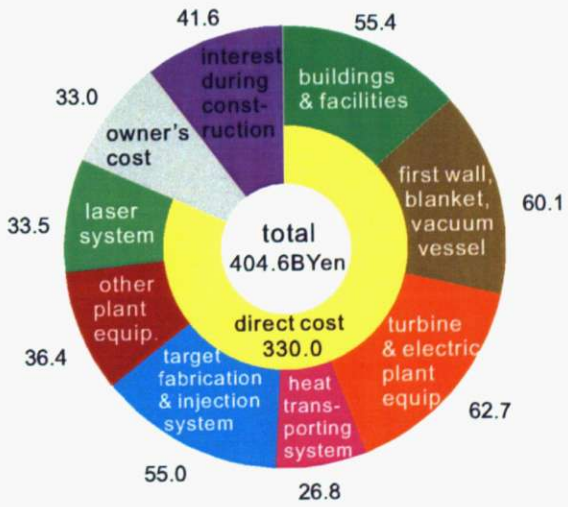

Fig. 6.1: Circle chart of breakdown cost

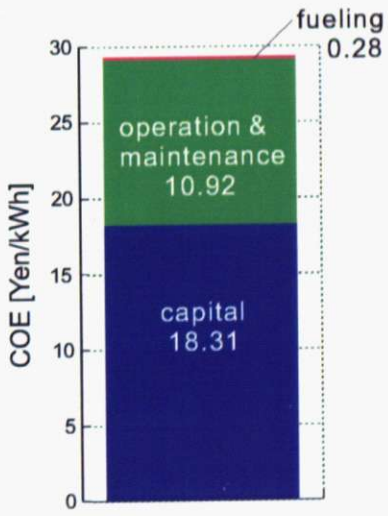

Fig. 6.2: Stacked bar chart of COE

Chapter 7

Discussion

7.1 Comparison with other IFE reactors

Since this design adopts a dry wall chamber, it is free from difficulties required for the development of a liquid wall. One of the main technological problems of a liquid wall is the limit in the selection of the structural material. The structural material must have not only compatibility but also good wettability with a liquid metal. In the design of KOYO and KOYO-Fast reactor the use of silicon carbide (SiC) is assumed. SiC is already used in aerospace field as a part of structural material because of its high strength despite its light weight. However, SiC has not yet been used in a nuclear reactor, in which the material is exposed to a constant high heat and neutron flux. Recently, SiC components made by NITE (Nano-Infiltration and Transient Eutectic phase) process has attracted attention because it shows quite good irradiation properties [77]. But still some problems remain to fabricate large and complicated components. A liquid wall chamber also has a problem in covering its ceiling. In ARIES-IFE design study [78], two methods are considered to cover the ceiling; forced flow along the ceiling, slowly permeates liquid metal into porous structural material. But it requires additional engineering development and the repetition rate of laser irradiation also limited within a certain range to keep good thin liquid layer. In the design of KOYO-Fast, the ceiling is expected to be protected by the thin liquid layer which is condensed from the metal vapor in the chamber by keeping the ceiling away from the chamber center and cooling it. But in this scheme the shape of the chamber is vertically long (about 10 m in the vertical direction, whereas the chamber radius is 4 m), which leads to the increase of the total weight. A liquid wall can accommodate much higher heat than a dry wall. But it also means that if a dry patch is emerged the region is severely damaged. The design study of KOYO-Fast indicates that the possibility of such direct exposure must be less than $1/10^4$ [79]. For 4 Hz repetition, this condition coincides dry patch generation for longer than 0.25 sec is not allowed in any 40 minutes during operation for several years.

The design with a dry wall is free from such technological problems accompanied with the use of a liquid wall. However, a dry wall may undergo large plastic deformation that leads to low cycle fatigue. It can also undergo the mass loss of the surface layer by exfoliation due to the accumulation of helium. In the HAPL project, the magnetic intervention method [9] has been considered to be the most probable option because it is thought to be difficult to suppress these threatening effects. In this design we adopts fast ignition scheme and the target yield is minimized. Then maximum surface temperature is much less ($\sim$ 1600 K) than HAPL ($\sim$ 2300 K) and many alternative materials except for tungsten and CFC can be a candidate for the first wall armor. However, as shown in chapter 5, even with this minimized target yield, plastic deformation is still a concern for the compact chamber that can be replaced by the cask method. In addition, the threatening effects due to the irradiation of energetic particles are not alleviated by minimizing the target yield because these spectrum do not change so much with the target yield. Then helium accumulation causes a serious problem. Although it is indicated that several highly-engineered materials can suppress the helium concentration, several technological development is required for the use of such advanced materials for large area of the chamber first wall. Then in the development of laser fusion reactors, the difficulties in the development of a liquid wall system and the mass-production of highly-engineered materials for dry wall material must be compared each other.

Since this design adopts fast ignition scheme, the feasibility of effective heating that leads to ignition and burn is one of the critical factor. Present experimental data were obtained from the pellet of which areal density value is almost the same that required for the ignition condition. Then experimental demonstration of fast heating of the small portion of a big pellet is expected. When fast ignition scheme is adopted, there is no difference in the core plasma physics between a liquid wall concept and dry wall concept. However, as shown in chapter 6, it is possible that the cone-shape laser guide cannot be used in a dry wall chamber. Then the feasibility of efficient core heating without cone guide becomes the critical factor for the dry wall design. In this design relatively small pellet compared with other reactor design studies were used. Then the extrapolability of the numerical results of pellet implosion in other works was also concerned. But as shown in chapter 4, numerical simulation indicates that the pellet is expected to be compressed as much density as the large one and sufficient gain can be obtained. Then it is expected that we can refer to the result of other optimization study for pellet design and laser pulse shaping. We also expected that the adoption of fast ignition enabled slow implosion which is favorable from the view point of suppressing the R-T instability during the implosion. Contrary to the expectation, no distinct difference was observed in the growth rate of R-T instability among the pellets with different initial aspect ratio. But these growth rates do not deny the feasibility of a small yield

target, rather indicates the robustness of the pellet design.

From the viewpoint of the maintenance, this dry wall design has a merit that it can adopt a simple cask method. A liquid wall chamber also needs to be replaced periodically because of the neutron damage of its structural material. In the design of KOYO-Fast reactor, the method of sector division of the chamber is considered but the detailed maintenance scheme has not yet been discussed. Compared with HAPL, which also adopts dry wall chamber, this design still has two advantages. The one is the high accessibility of maintenance tools because of the small number of laser beams. The other is the less weight of total blanket system because of the smaller chamber radius. These advantages lead to less maintenance time and reduction of the size of maintenance tools and maintenance room.

As shown in chapter 6, the cost of electricity (COE) of a dry wall reactor is about 30 yen/kWh. Table 7.1 shows the comparison of cost parameters for this design (FALCON-D), KOYO, KOYO-Fast and HAPL. Here the parameters of KOYO-Fast showed in the table are estimated values by the developed system code because cost analysis result of KOYO-Fast presently is not available. The cost parameters for HAPL is also derived from the plant design which is slightly different from the finalized one. Thus note that readers should use these values only as a guide. One can easily seen the total plant capital cost and the laser system cost of FALCON-D are smaller than other designs. Nevertheless, the COE of FALCON-D is much higher than other designs due to its small electric output. Of course the value of COE strongly depends on the cost model used in the calculation. For example, the difference in the maintenance scheme is expected to be affect the cost. In this analysis such difference is not considered. However, this big difference in COE between FALCON-D and the other designs cannot be reduced even if the detailed cost model is considered. Therefore we need to weigh the advantage of a compact dry wall design (e.g., small construction cost, easiness in maintenance, etc.) and the disadvantage of the high COE in the consideration of the guideline of development and operation of this design.

7.2 Comparison with a magnetic fusion reactor

It is also important to compare this design with a magnetic confinement fusion reactor. In a magnetic fusion reactor, the first wall is not exposed directly the energetic charged particle because of the existence of strong magnetic field. Most particle and heat flux strike a divertor plate located on the bottom of the vacuum chamber and neutralizes plasma including impurities for effective evacuation, Then a divertor plate is exposed to a constant high ($\sim$ 1–10 MW/m^2) heat flux. In addition, a divertor plate also undergoes several intermittent heat injection processes. Table 7.2 shows the characteristics of such heat injection processes in ITER. For comparison, characteristics of the heat injection to the first wall of

Table 7.1: Comparison of cost parameters of IFE reactor designs (Unit:Byen)

	FALCON-D	KOYO	KOYO-Fast[a)]	HAPL[b)]
chamber radius [m]	5.64	3	4	11
net electric output [MWe]	396	2840	1200	1000
buildings and facilities	55.4	74.2	36.4	47.8
first wall, blanket, vacuum vessel etc.	60.1	61.3	38.1	23.9
turbine and electric plant equipment	62.7	250.6	144.7	79.8
heat transportation system	26.8	137.8	81.7	74.5
target fabrication and injection system	55.0	–[c)]	–[c)]	17.8
other plant equipments	36.4	101.2	66.9	48.6
laser system	33.5	140.0	42.8	74.5
direct cost	328.8	765.2	410.6	367.3
owner's cost	32.9	76.5	41.1	36.7
interest during construction	41.4	106.0	51.7	46.2
total plant capital cost	403.2	947.8	503.4	450.2
COE [yen/kWh]	29.51	7.94	11.10	8.50

a) estimated by using the system code developed in this research.
b) calculated from the value in reference [80] and assuming $1=110 yen.
c) In KOYO and KOYO-Fast design the pellet manufacturing cost is assumed to be 16 yen per one pellet and reflected in the calculation of annual fueling cost.

FALCON-D is also shown. As you can see, the total energy amount of each heat injection process in magnetic fusion reactor exceeds that of an IFE reactor. Then melting or ablation of surface layer of the divertor plate is inevitable when such large heat flux is injected. Therefore the possible material for the armor of the divertor is tungsten or CFC considering its high melting (sublimation) point. Whereas in our design, as mentioned in the above, many alternative materials can be used.

An IFE first wall undergoes a repetitive heat load and fatigue failure due to a cyclic deformation is strongly concerned. A magnetic fusion reactor can also undergo a periodic heat load by ELM (Edge Localized Mode). ELM is the instability growing at the edge region of a plasma with the improved confinement mode (H-mode). H-mode plasma has a transportation barrier (called as 'pedestal structure') with high pressure gradient at the edge region. When ELM occurs the pedestal structure collapses with ejection of heat and particles from the main plasma and after that the pedestal structure is recovered. Though this periodic repetition of collapse and recovering slightly reduced the energy confinement (about 80 % of that without ELM), it can remove impurities including helium ashes from main plasma. This fairly good confinement with the removal of impurities is suitable for steady state operation and the operation in H-mode with ELM (ELMy H-mode) is considered to be a standard operation mode for ITER. The pulse width of ELM is about 100 times longer than that of an IFE reactor. The characteristic length ℓ of heat diffusion can be estimated by the square root of the product of thermal diffusion coefficient and the pulse width $\ell \sim \sqrt{\kappa t}$. However ELM also causes intermittent temperature

increase of the surface considering its large heat amount and the short heat deposition depth. Thus it also can cause a cyclic deformation of the surface. There are several types of ELM is observed in the experiment. Type-I ELM is the most frequent observable mode in Tokamak reactor and has good pedestal which can keep a good confinement. But if assuming the total energy amount released in one pulse of Type-I ELM is proportional to the stored energy of the plasma, the energy injected into divertor plate during one pulse ELM can reach 10 MJ for ITER, that inevitably leads to melting, and ablation of a part, of the divertor material even if tungsten is used. Then in a operation of a commercial reactor, suppression of Type-I ELM is one of the critical issue. It has been found several operation modes of H-mode with ELM of which amplitude is much less than Type-I ELM or without any ELM [81]. If the operation without ELM is achieved, a magnetic fusion reactor is free from the cyclic deformation.

A divertor plate is also exposed to a particle irradiation. The flux of particle is much higher than that in the case of an IFE reactor. But in the case of divertor plate, the energy of particles are $\sim$ 1 keV, much less than that of an IFE reactor case ($\sim$ 1 MeV). Then the range of particles is also shorter (several tens nanometer). The impurities in the divertor armor can easily move to the surface by this short range and relatively long pulse width. The experiment in Nagoya University [82] showed that the helium bubbles were disappeared after the irradiation of ruby laser, which has relatively long pulse width of 0.3 ms. This alleviation effect cannot be expected under an IFE condition.

Table 7.2: A comparison of the characteristics of pulse heat injection process in magnetic fusion experimental reactor ITER and laser fusion reactor design FALCON-D

	ITER Type-I ELM	ITER Vertical Displacement Event	ITER Disruption	FALCON-D first wall
Energy	$\sim$ 10 MJ	$\sim$ 50 MJ/m^2	$\sim$ 100 MJ	0.02 MJ/m^2
Affected area	5–10 m^2	$\sim$ 1 m^2	$\sim$ 10 m^2	whole chamber w all
Time	$\geq$200 μs	$\sim$ 0.3 s	$\sim$ 1 ms	2 μs
Frequency	few Hz	$\sim$ 1/100 discharges	$\sim$ 1/10 discharges	30 Hz
Heat flux [W/cm^2]	10^5-10^6	$\sim 10^4$	$\sim 10^6$	$\sim 10^6$
Particle flux		$\sim 10^{24}$m^{-2}s^{-1}		$\sim 10^{19}$ m^{-2} s–1

From the viewpoint of the plasma physics, implosion of the fuel pellet has been studied intensely and accurate prediction can be given by a numerical simulation. Whereas the detailed mechanism of fast heating is still unknown because it contains many complicated physics processes including relativistic interaction of ultra-intense laser with extremely dense core plasma. At present many theoretical and numerical works are carried out to clarify this process [83]. But an experimental demonstration is also necessary. Thus progress in the experimental study (e.g., FIREX (Fast Ignition REsearch eXperiment) in Osaka University) is strongly expected.

Blanket system and shield is common with a magnetic fusion reactor. Then the technology developed in a magnetic fusion research can be applied in the design of an IFE reactor. Rather an IFE reactor has a couple of merits. Since an IFE reactor does not have any magnetic field in the blanket, then a liquid blanket is free from the MHD pressure loss. An IFE reactor also does not have superconducting coil around the vacuum chamber and neutron flux inevitably passes beam ports and can reach reactor room by penetrating beam ducts. Then reactor room needs to be served as a neutron shield, i.e., no need of a thick shielding material in the vacuum vessel. This property enables the simple maintenance method, extraction of blanket system to upper direction, as shown in chapter 3.

From the view point of the maintenance, an IFE reactor requires the maintenance of the final optics system. The mechanics like a rotating shutter is also needed to avoid the direct irradiation of energetic particle on the final optics. These technology is not required in a magnetic fusion reactor, thus simultaneous development of such components is required with the experimental research of the fast ignition.

One of the remarkable differences in a magnetic fusion and inertial fusion is the design possibility of medium scale plant. In magnetic fusion, if the volume of plasma is reduced to decrease fusion output, the confinement deteriorates. Then there is a lower limit in the plasma volume. In addition, the size of a magnetic fusion reactor depends on not only the plasma volume but also the volume of coil windings and coil casing. Then the major radius (the distance between the center of the device and the toroidal magnetic axis) cannot be reduced so much as the reduction in the plasma minor radius. Figure 7.1 shows the dependence of COE on the electric output for a magnetic fusion reactor and an IFE reactor. The plant design parameters of PPCS model A [84], the commercial plant designed by EU, was used as a base parameter set for the magnetic fusion reactor. Here chamber radius of the IFE reactor was determined so that the wall heat load is the same value as that of FALCON-D. Plasma major radius of the magnetic fusion reactor was selected so that the confinement improvement factor for IPB98 scaling H_H is the same value as the PPCS model A ($H_H \sim 1.2$). For comparison, COE is normalized by the value with the electric output of 1000 MWe (103 mill/kWh for magnetic fusion, 19.1 yen/kWh for IFE). As you can see, a magnetic fusion reactor has stronger advantage of scale than an IFE reactor. Conversely, an IFE reactor has a possibility in the design of a smaller scale plant. This characteristic, as well as the easiness in varying its output by adjusting the laser repetition rate, should be remarked because it can lead to the flexibility in the operation as a power plant. This fact indicates the possibility that a magnetic fusion reactor and an IFE reactor are complementary to one another in an electric market. It can be said that it is importance to consider this fact in the research and development of

fusion energy source.

7.3 Required issues in research and development

As described in this chapter and chapter 5, the design feasibility of a laser fusion reactor with a dry wall chamber totally depends on the possibility of the development of the first wall material that can avoid low cycle fatigue and exfoliation due to helium concentration. Some highly-engineered materials are probable candidate, but the test under the actual IFE condition is necessary to confirm the feasibility. Then the progress in the experiment that enables fusion burn of the pellet and provides the same environment in the reactor chamber to the candidate material for the first wall armor (e.g., NIF (National Ignition Facility) in LLNL (Lawrence Livermore National Laboratory, US) and FIREX in Osaka University) is strongly expected. It is also expected to establish reliable database of thermo-mechanical properties of candidate materials (especially in high temperature region) by using present several ion/laser irradiation facilities. These experimental studies also contribute to the development of a magnetic fusion research.

Other critical factor to achieve a dry wall chamber is the demonstration of the sufficient high gain achievement by using fast ignition method without a cone guide. Fast ignition with cone guide is expected to be demonstrated in FIREX project. At present fast ignition without cone guide is also studied as mentioned in chapter 6, but further research in a large experimental facility is expected.

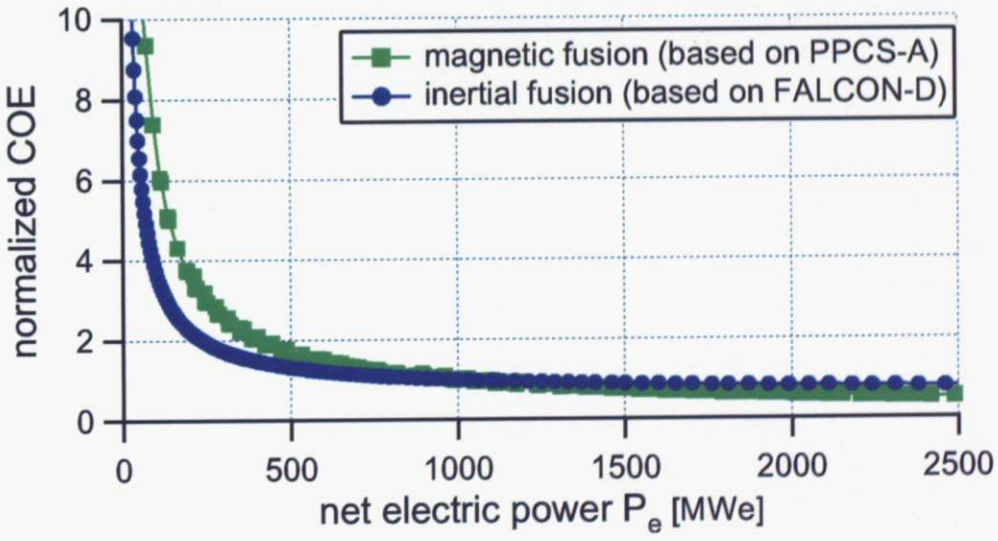

Fig. 7.1: Comparison of COE dependence on electric power output between a magnetic fusion reactor (based on PPCS model-A) and an IFE reactor (based on FALCON-D). COE is normalized by its value at the net electric power of 1 GWe.

This dry wall design requires the sufficiently high gain with a small target yield. Then a novel idea to achieve ignition, impact ignition [85], also provides a possible scenario. Impact ignition scheme aims high gain achievement by colliding an accelerated fuel portion, call an "ignitor", to a compressed fuel (see Fig. 7.2). To achieve high gain, ignitor must have a extremely high speed ($\sim$ 1000 km/s) and high density (several g/cm^3) simultaneously immediately before the impact collision. Then at present cone guide like the fast ignition is used to converge fuel during acceleration. But in principle impact ignition can be achieved without a cone guide. Impact ignition also needs no ultra-intense laser. Then it is expected that high repetition rate with a cone guide is also possible because all beams can work as an acceleration beam. Thus the progress in the research of impact ignition is also expected.

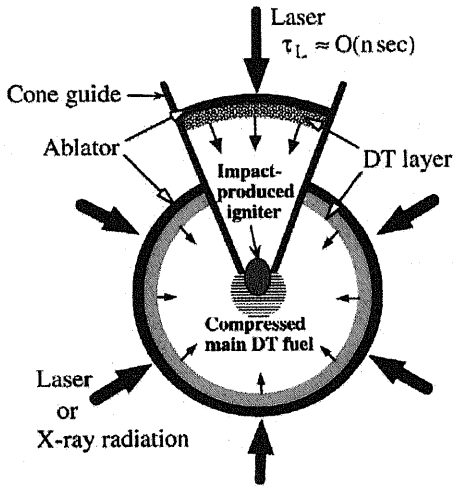

Fig. 7.2: Schematic view of the fuel pellet for the impact ignition (Fig. 1 of reference [85]).

Of course intense researches have already been carried out in both fields. But if the design feasibility of a laser fusion reactor with a compact dry wall chamber is confirmed, it make a great impact on the development of a magnetic fusion as well as an IFE. Thus further study that considers the final design of a commercial fusion plant is strongly expected.

Chapter 8

Conclusion

The design study of fast ignition laser fusion plant with a dry wall chamber has been carried out. Key points in this design is to explore the design that makes the full use of the fast ignition scheme. For example;

- Core plasma design by utilizing the alleviation on the physics requirement in the pellet implosion
- Dry wall chamber design by utilizing relatively low wall load

In the design of core plasma, the optimum design of pellet and laser pulse shaping for a pellet implosion has been examined by using one dimensional hydrodynamic code ILESTA-1D. The facts clarified by this research are:

- The coupling efficiency of implosion laser and isentrope factor are in the range of 0.03-0.05 and 2-2.5, respectively. These values lead to pellet compression with lower average density than that predicted in zero-dimensional physics model.
- Despite of low average density, the areal density value at the timing of the maximum compression is almost the same value expected in zero-dimensional model by the enhancement effect on the areal density due to the density peaking.
- The maximum areal density does not depend so much on the initial aspect ratio of the fuel pellet. Whereas the peak density at the maximum compression increases with increasing the initial aspect ratio.
- The growth rate of Rayleigh-Taylor instability during implosion also does not depend so much on the initial aspect ratio.

These results surely showed the effectiveness, but not superiority, of slow implosion. We also tried to simulate fast ignition effect by adding the artificial heating to the electron in the compressed core plasma.

Although this method can reproduce the effect of external heating, it is clarified that the difference of temperature and density profile in the heating region strongly affects the heating and burning properties. Then we carried out two dimensional hydrodynamic simulation and the following facts are clarified:

- there is a threshold heating energy for ignition and burn of the compressed fuel.
- this threshold energy only depends on the peak density of the compressed fuel and the energy decreases with increasing of the peak density

Thus from the viewpoint of simultaneous achievement of high hydrodynamic stability in the implosion and high density compression, which leads to the reduction of heating energy, higher initial aspect ratio is favorable within the simple laser pulse shaping based on the theory of isentropic compression of hollow shell. However, high peak density also means steep density gradient between the high density cold fuel and the relatively high temperature, low density center region at the maximum compression. This may lead to mixture of both regions due to the growth of R-T instability at stagnation phase. This fact might give an upper limit of the initial aspect ratio. The peak density also increases by increasing the peak power of the implosion laser. In the case of implosion of the pellet of which initial aspect ratio is 4 by a 350 kJ implosion laser with the peak power of 120 TW, the peak density reaches to 800 g/cm^3. Then pellet gain $G = 100$ is achieved with the net core heating energy of 10 kJ. This result indicates if the coupling efficiency of heating laser to the compressed core can be 20 %, the sufficient high gain achievement with 400 kJ laser (350 kJ for implosion and 50 kJ for heating). Therefore the design point of FALCON-D, estimated by the simple 0-D physics model, was successfully demonstrated.

In the feasibility study of a dry wall chamber, tungsten-armed reduce activated ferritic steel (F82H) was selected to be a candidate of the first wall material and temporal evolution of temperature and thermal stress and strain was investigated by using the developed one-dimensional thermal analysis code and commercial FEM code ANSYS. In addition, other threatening effects caused by particle irradiation (e.g., sputtering, blistering, carbide formation) were also considered in as quantitative way as possible. These analyses revealed that the temperature increase is not concern in the case of chamber radius of 5.64 m and 30 Hz repetition. However, the surface of the first wall can undergo large plastic deformation and low cycle fatigue failure is much concerned. But in an IFE condition, the strain rate is very high ($\sim 10^4$/s) due to the short heat pulse ($\sim 1musec$) and the deformation mechanism is quite different from the static deformation. In this case the yielding stress becomes a few times higher than static case and this yielding stress also depends on the grain size of the materials. Then fine-grained material can avoid the plastic deformation. From the viewpoint of high energy particle load, the sputtering effect is negligible. However, the mass loss of the armor material through blistering and surface exfoliation due

to helium accumulation can also be a considerable problem. These results indicate the difficulties in a dry wall chamber design even under condition of much lower heat load that is achieved by the utilization of the fast ignition scheme. Here some highly-engineering materials (e.g., tungsten foam or carpet, and ultra fine-grained tungsten (UFG-W)) can be a solution of the dry wall chamber design. Especially, UFG-W has almost three times higher yielding stress at high strain-rate deformation compared with that of as-received tungsten in static deformation UFG-W also has very high recrystallization temperature and good irradiation property. In addition, it is known that UFG-W has two order or more higher threshold value of helium fluence to cause blistering. Then UFG-W is expected to be a most possible candidate for the first wall armor material.

According to these detailed analysis of core plasma and the dry wall, the design possibility of a commercial laser fusion plant with a dry wall chamber was shown. By increasing the repetition rate of laser irradiation to 30 Hz, net electric output of 400 MWe is achievable in this design. Although the cost of electricity of the proposed design is much higher than that of current commercial plant due to the small electric output, its relatively low construction cost and high engineering feasibility and reliability provide favorable option for the laser fusion plant.

To confirm the feasibility of this dry wall design, experimental demonstration of the dry wall survival under an IFE condition and the effective heating by fast ignition scheme without cone guide are indispensable. These achievement, especially the former, can make a great contribution on not only inertial but also magnetic fusion research and development. Then intensive study in such experimental demonstration and establishment of reliable database are strongly expected.

Acknowledgement

First of all, and most importantly of all, I'd like to express my great gratitude to Professor Yuichi Ogawa, my direct supervisor in the laboratory. He have instructed me over a period of 5 years. He always cared about me and provided pointed advises when I faced difficulties. I cannot carry out this work without his supports. I also appreciate to Professor Zensho Yoshida and Associate Professor Masaru Furukawa for their insightful comments. Dr. Junji Morikawa and Dr. Haruhiko Saito always cared me. I also would like to thank them.

I also thankful to the all members in the laboratory. Especially, Mr. Daisuke Ninomiya gave a significant assistance to the introduce and the revision of the hydrodynamic code ILESTA-1D. Mr. Toru Terai made a great contribution to the refinement of the system code. Mr. Eiichi Yatsuka often had a discussion with me despite the difference in the field of research. Mr. Sho Watanabe, Mr. Shuhei Numazawa, Mr. Yoshihisa Yano, Mr. Daisuke Sakata, Ms. Junko Suzuki, Mr. Yohei Kimura, Mr. Kiyotake Kinjo, Ms. Tomoyo Nakatsu, Mr. Hiroyuki Hayashi, Mr. Naoki Shinji and Mr. Shota Tanaka also helped me in many aspects of daily life.

Many researchers in other laboratories significantly contributed to this work. Dr. Kunihiko Okano, Dr. Yoshiyuki Asaoka and Dr. Ryoji Hiwatari in Central Research Institute of Electric Power Industry (CREPI), and Mr. Youji Someya in Musashi Institute of Technology often had discussions with me and gave a lot of advises on this work as a collaborator. Professor Kazuo A. Tanaka in Osaka University provides a lot of information about the recent issues in the fast ignition research. He also kindly taught me about the basic idea of the thermal analysis of a dry wall. Dr. Hiroyuki Furukawa in Institute of Laser Technology advised me about the thermal analysis and provided a lot of documents. Professor Hideaki Takabe and Professor Hiroshi Azechi in Osaka University gave a great help in the introduce of ILESTA-1D. Dr. Atsushi Sunahara in Institute of Laser Technology kindly gave a lot of instructions in the introduce and operation of ILESTA-1D and had a lot of discussion about the hydrodynamics in the implosion process. Dr. Tomoyuki Johzaki in Institute of Laser Engineering, Osaka University also had a lot of discussion about the fast heating and burn of the fuel pellet. He also kindly carried out 2-D

calculations for this work out of his busy schedule. Drs. Mikio Enoeda and Satoshi Suzuki in Japanese Atomic Energy Agency (JAEA) provided valuable informations about the mechanical analysis. Professor Yoshio Ueda in Osaka University kindly had a discussion with me about the thermomechanical analysis. Professor Naoaki Noshida in Kyushu University provided a number of informations and documents about the irradiation effect of tungsten. Associate Professor Hiroaki Kurishita provided the recent information about ultra-fine grained materials. Dr. A. René Raffray in the University of California, San Diego (UCSD) instructed me with a great kindness during my stay in UCSD. He took much time to discuss with me and provided valuable informations. Dr. Farrokh Najmabadi, Dr. Mark S. Tillack and Dr. T. K. Mau in UCSD also cared me and gave me pointed comments. Dr. John E. Pulsifer and Dr. Lane Carlson kindly guided me the laser laboratory "dragonfire" in UCSD. Dr. Shahram Sharafat in the University of California, Los Angels (UCLA) provides a lot of information about the dry wall armor design. Unfortunately I cannot meet him but he kindly took time from his busy schedule to discussed long time with me over the phone. I'd like to express my gratitude for all these researchers.

I also thanks the all people who support my daily life. Ms. Sunami Kojima and Ms. Nami Sugimura provided heartily support in daily life in the laboratory. Ms. Cynthia Escobedo kindly made the all arrangement needed before my visit to UCSD. Ms. Tencer Vickie arranged the all office procedures during my stay in UCSD. The family who rent a room of their apartment for me in San Diego, Ms. Agnes Ong, Mr. Edward Liaw and Mr. Laymond Liaw, are all very hospitable to me despite of very short stay. I also appreciate to Dr. Jun-ya Shiraishi, my senior in the laboratory and who works at General Atomics in San Diego, and his wife for their kindness to guide and help in the arrangement of daily necessaries.

This work also supported in part by the Global COE (GCOE) Program on the Nuclear Education and Research Initiative of The University of Tokyo and Japan-US Fusion Research Cooperative Program of National Institute of Fusion Science (NIFS) and Japan Society for the Promotion of Science (JSPS). I would like to take this opportunity to thank the entire members who are relevant to these programs.

Last of all, I really to appreciate my parents, who always care me despite living away, and my loved wife Kuniko, who provides emotional support every day.

Bibliography

[1] F. Najmabadi and The Aries Team, "Overview of the ARIES-RS reversed-shear tokamak power plant study", Fus. Eng. Des. **38** (1997) 3-25.

[2] A. Sagara, K. Y. Watanabe, K. Yamazaki *et al.*, "LHD-Type Compact Helical Reactors", *Proc. 16th Conf. on IAEA Fusion Energy Conference*, Yokohama, Japan, October 19-24th, 1998, IAEA-CN69/FTP3/03.

[3] S. Nishio, K. Ushigusa, S. Ueda *et al.*, "Conceptual Design of Advanced Steady-State Tokamak Reactor –Compact and Safety Commercial Power Plant (A-SSTR2)–", *Proc. 18th Conf. on IAEA Fusion Energy Conference*, Sorrento, Italy, October 4-10th, 2000, IAEA-CN77/FTP2/14.

[4] K. Okano, Y. Asaoka, T. Yoshida *et al.*, "Compact Reversed Shear Tokamak Reactor with a Superheated Steam Cycle", Nucl. Fusion **40** (2000) 635-646.

[5] F. Najmabadi and The Aries Team, "The ARIES-AT advanced tokamak, Advanced technology fusion power plant", Fus. Eng. Des. **80** (2006) 3-23.

[6] Conceptual Design of Laser Fusion Reactor 'KOYO', Institute of Laser Engineering (ILE), Osaka University, 1995.

[7] Conceptual Design of Fast Ignition Laser Fusion Electric Power Plant, Institute of Laser Engineering (ILE), Osaka University, 2006.

[8] J. D. Sethian, A. R. Raffray, J. Latkowski *et al.*, "An overview of the development of the first wall and other principal components of a laser fusion power plant", J. Nucl. Mater. **347** (2005) 161-177.

[9] A. R. Raffray, J. Blanchard, A. E. Robson *et al.*, "Impact of Magnetic Diversion on Laser IFE Reactor Design and Performance", J. Phys. IV France **133** (2006) 845-848.

[10] G. S. Fraley *et al.*, "Thermonuclear burn characteristics of compressed deuterium-tritium microspheres, Phys. Fluids **17** (1974) 474.

[11] E. N. Avororin, L. P. Feoktistov and L. I. Shibarshov, "Ignition criterion for pulsed fusion targets", Sov. J. Plasma Phys. **6** (1980) 527-531.

[12] S. Skupsky, "Energy Loss of Ions Moving through High-density Matter", Phys. Rev. A **16** (1977) 727.

[13] R. E. Kidder, "Laser-driven Isentropic Hollow-shell Implosions: The Problem of Ignition", Nucl. Fusion **19** (1979) 223.

[14] M. Murakami and K. Nishihara, "Efficient Shell Implosion and Target Design", Jpn. J. Appl. Phys. **26** (1987) 1132.

[15] H. Takabe *et al.*, "Self-consistent growth rate of the Rayleigh-Taylor instability in an ablatively accelerating plasma", Phys. Fluids **28** No. 12 (1985) 3676.

[16] H. Takabe, "Inertial Confinement Fusion and Supernova Explosion", JSPF **69** 1285 (1993) [*in japanese*].

[17] "*Energy from Inertial Fusion*", International Atomic Energy Agency, (1995).

[18] W. L. Kruer and K. Estabrook, "$J \times B$ heating by very intense laser light", Phys. Fluids **28** (1985) 430-432.

[19] F. Brunel, "Not-so-resonant, resonant absorption", Phys. Rev. Lett. **59** (1987) 52-55.

[20] D. Strickland and G. Mourou, "Compression of amplified chirped optical pulses", Opt. Commun. **56** (1985) 219-221.

[21] M. Tabak, J. Hammer, M. E. Glinsky *et al.*, "Ignition and high gain with ultrapowerful lasers", Phys. Plasmas **1** (1994) 1626-1634.

[22] R. Kodama, P. A. Norreys, K. Mima *et al.*, "Fast heating of ultrahigh-density plasma as a step towards laser fusion ignition", Nature **412** (2001) 798-802.

[23] R. Kodama, H. Shiraga, K. Shigemori *et al.*, "Fast heating scalable to laser fusion ignition", Nature **418** (2002) 933-934. Chamber and Driver Design for Heavy Ion Inertial Fusion Energy", Fusion Tech. **46** (2004) 470. Reactor Design", Nucl. Tech. /Fusion **1** (1981) 302.

[24] H. S. Bosch and G. M. Hale, "Improved Formulas for Fusion Cross-sections and Thermal Reactivities", Nucl. Fusion **32** (1992) 611.

[25] V. A. Chuyanov, "ITER Test Blanket Working Group activities: a summary, recommendations and conclusions", Fus. Eng. Des. **61-62** (2002) 273-281.

[26] Y. Someya, T. Matsumoto, R. Hiwatari *et al.*, "Preliminary Neutronics Analysis and Maintenance Approach for Final Optical Devices of Fast Ignition ICF Reactor FALCON-D", To be published in Fus. Eng. Des. .

[27] M. Murakami, K. Nishihara and H. Azechi, "Irradiation nonuniformity due to imperfections of laser beams", J. Appl. Phys. **74** (1993) 802-808.

[28] Y. Asaoka, R. Hiwatari, K. Okano *et al.*, "Conceptual design of a demonstration reactor for electric power generation", *Proc. 20th IAEA fusion energy conference*, Vilamoura, Portugal, Nov. 1-6, 2004, FT/P7-4.

[29] L. M. Waganer, "ARIES-AT maintenance system definition and analysis", Fus. Eng. Des. **80** (2006) 161-180.

[30] T. Nishitani , E. Inshitsuka , T. Kakuta *et al.*, "Japanese contribution to ITER task of irradiation tests on diagnostics components", Fus. Eng. Des. **42** (1998) 443-448.

[31] R. M. More, K. H. Warren, D. A. Young, and G. B. Zimmerman, "A New Quotidian Equation of State (QEOS) for Hot Dense Matter", Phys. Fluid **31** (1988) 3059-3078.

[32] K. Takami and H. Takabe "Simple Fitting Formulas of Equation of State for Laser Produced Plasmas", Technology Reports of the Osaka University **40** (1990) 159-173.

[33] E. G. Corman, W. E. Loewe, G. E. Cooper and A. M. Winslow, "Multi-Group Diffusion of Energetic Charged Particles", Nucl. Fusion **15** (1975) 377-386.

[34] R. E. Kidder, "Theory of Homogeneous Isentropic Compression and Its Application to Laser Fusion", Nucl. Fusion **14** (1974) 53-60.

[35] R. E. Kidder, "Laser-driven Compression of Hollow Shells: Power Requirements and Stability Limitations", Nucl. Fusion **16** (1976) 3-14.

[36] R. Betti, V. N. Goncharov, R. L. McCrory, and C. P. Verdon, "Growth rates of the ablative Rayleigh-Taylor instability in inertial confinement fusion", Phys. Plasmas **5** (1998) 1446-1454.

[37] W. K. Levedahl and J. D. Lindl, "Energy Scaling of Inertial Confinement Fusion Targets for Ignition and High Gain", Nucl. Fusion **37** (1997) 165-173.

[38] M. M. Basko and J. Johner, "Ignition Energy Scaling of Inertial Confinement Fusion Targets", Nucl. Fusion **38** (1998) 1779-1788.

[39] M. C. Herrmann, M. Tabak and J. D. Lindl, "A generalized scaling law for the ignition energy of inertial confinement fusion capsules", Nucl. Fusion **41** (2001) 99-111.

[40] R. Betti, A. A. Solodov, J. A. Delettrez and C. Zhou, "Gain curves for direct-drive fast ignition at densities around 300 g/cc", Phys. Plasmas **13** (2006) 100703.

[41] Summary of ITER final design report, (2001).

[42] M. Kikuchi, JA-EU satellite tokamak working group and JT-60SA design team, "Overview of Modification of JT-60U for the Satellite Tokamak Program as one of the Broader Approach Projects and National Program", *Proc. 21th Conf. on IAEA Fusion Energy Conference*, Chengdu, China, October 16th-21st, 2006.

[43] Y. S. Touloukian *et al.*, *Thermophysical Properties of Matter*, The TPRC Data Series, New York:IFI/Plenum, (1970).

[44] J. F. Shackelford, *CRC materials and engineering handbook*, Boca Raton, CRC Press (1994).

[45] B. L. Henke, E. M. Gullikson and J. C.Davis, atomic data and nuclear data tables **54** (1993) 181-342.

[46] J. F. Ziegler, "The Stopping of Energetic Light Ions in Elemental Matter", J. Appl. Phys. **85** (1999) 1249-1272: the SRIM code is available from ⟨http://www.srim.org⟩

[47] J. D. Sethian, A. R. Raffray, J. Latkowski *et al.*, "An overview of the development of the first wall and other principal components of a laser fusion power plant", J. Nucl. Mater. **347** (2005) 161-177.

[48] J. P. Blanchard and C. J. Martin, "Thermomechanical effects in a laser IFE first wall", J. Nucl. Mater. **347** (2005) 192-206.

[49] J. F. Stubbins and D. S. Gelles, "Fatigue performance and cyclic softening of F82H, a ferritic-martensitic steel", J. Nucl. Mater. **233-237** (1996) 331-335.

[50] C. Petersen and D. Rodrian, "Thermo-mechanical fatigue behavior of reduced activation ferrite/martensite stainless steels", J. Nucl. Mater. **307-311** (2002) 500-504.

[51] Y. Miwa, S. Jitsukawa and M. Yonekawa, "Fatigue properties of F82H irradiated at 523 K to 3.8 dpa", J. Nucl. Mater. **329-333** (2004) 1098-1102.

[52] T. Dümmer, J. C. Lasalvia, G. Ravichandran and M. A. Meyers, "Effect of strain rate on plastic flow and failure in polycrystalline tungsten", Acta. Mater. **46** (1998) 6267-6290.

[53] G. Subhash, Y. J. Lee and G. Ravichandran, "Plastic deformation of CVD textured tungsten—I. Constitutive response", Acta. Metall. Mater. **42** (1994) 319-330.

[54] A. S. Khan and R. Liang, "Behaviors of three BCC metal over a wide range of strain rates and temperatures: experiments and modeling", Int. J. Plastic. **15** (1999) 1089-1109.

[55] D. Hull, "Effect of Grain Size and Temperature on Slip, Twinning and Fracture in 3% Silicon Iron", Acta. Metall. **9** (1961) 191-203.

[56] C. A. Blue, V. K. Sikka, E. K. Ohriner *et al.*, JOM-e, **52** No. 1 (2000).

[57] H. Kim, J. El-Awady, J. Quan *et al*, "Failure Strength Measurements of VPS Tungsten Coatings for HAPL First Wall Armor", Fusion. Sci. Tech. **52** (2007) 875-879.

[58] Y. Yahiro, *in private communication.*

[59] Y. Yamamura and H. Tawara, "Energy Dependence of Ion-induced Sputtering Yields from Monoatomic Solids at Normal Incidence", Atomic Data and Nuclear Data Tables **62** (1996) 149-253.

[60] M. Poon, A. A. Haasz, J. W. Davis *et al.*, "Impurity effects and temperature dependence of D retention in single crystal tungsten", J. Nucl. Mater. **313-316** (2003) 199-203.

[61] S. B. Gilliam, S. M. Gidcumb, D. Forsythe, *et al.*, "Helium retention and surface blistering characteristics of tungsten with regard to first wall conditions in an inertial fusion energy reactor", Nucl. Instrum. Methods B **241** (2005) 491-495.

[62] S. B. Gilliam, S. M. Gidcumb, N. R. Parikh, *et al.*, "Retention and surface blistering of helium irradiated tungsten as a first wall material", J. Nucl. Mater. **347** (2005) 289-297.

[63] V. YA. Shchelkonogov, L. N. Aleksandrov, V. A. Piterimov and V. S. Mordyuk, "Internal friction method of studying the diffusion mobility of carbon in tungsten and molybdenum", Fiz. metal. Metalloved **25** (1968) 68-72.

[64] M. S. Abd El Keriem, D. P. van der Werf and F. Pleiter, "Helium-vacancy interaction in tungsten", Phys. Rev. B **47** (1993) 14771-14777.

[65] A. R. Raffray, "Engineering Analysis of He Retention and Release in Porous W Armor", Annual Report of UCSD CER (Center for Energy Research), UCSD-CER-05-09 (2005).

[66] S. Sharafat, N. M. Ghoniem, M. Anderson *et al.*, "Micro-engineered first wall tungsten armor for high average power laser fusion energy systems", J. Nucl. Mater. **347** (2005) 217-243.

[67] T. R. Knowles, "Tungsten Velvet Armor for HAPL Fusion Energy Systems", meeting documents of 15th HAPL meeting, General Atomics, San Diego CA, 8-9th August, 2006.

[68] T. B. Massalski, *Binary Alloy Phase Diagrams, 2nd ed.*, ASM, Metal Park, OH, 1990.

[69] H. Kurishita, Y. Amano, S. Kobayashi *et al.*, "Development of ultra-fine grained W-TiC and their mechanical properties for fusion applications", J. Nucl. Mater. **367-370** (2007) 1453-1457.

[70] J. S. Benjamin and T. E. Volin, "The Mechanism of Mechanical Alloying", Metal. Trans. **5** (1974) 1929-1934.

[71] H. Kurishita, S. Matsuo, H. Arakawa *et al.*, "Superplastic deformation in W-0.5 wt.% TiC with approximately 0.1 μm grain size", To be published in Mater. Sci. Eng. A.

[72] Q. Wei, T. Jiao, K. T. Ramesh *et al.*, "Mechanical behavior and dynamic failure of high-strength ultrafine grained tungsten under uniaxial compression"Acta Materialia **54** (2006) 77-87.

[73] T. Ogawa, *in private communication.*

[74] Y. Kozaki, "Research on System Design and Economic Evaluation of Laser Fusion Power Plants", Osaka University, (2003) [*in japanese*].

[75] Y. Kitagawa, Y. Sentoku, S. Akamatsu *et al.*, "Petawatt-laser direct heating of uniformly imploded deuterated-polystyrene shell target", Phys. Rev. E **71** (2005) 016403.

[76] R. Tsuji, "Trajectory adjusting system using a magnetic lens for a Pb-coated superconducting IFE target", Fus. Eng. Des. **81** (2006) 2877-2885.

[77] A. Kohyama, Y. Katoh, S. M. Dong *et al.*, *Proc. 19th IAEA Fusion Energy Conference*, Lyon, France, 14-19 October 2002, FTP1/02.

[78] M. Yoda, S. I. Abdel-Khalik and ARIES-IFE team, "An Investigation of the Fluid Dynamics Aspects of Thin Liquid Film Protection Schemes for Inertial Fusion Energy Reactor Chambers", Fus. Sci. Technol. **46** (2004) 451-469.

[79] T. Norimatsu, J. Kawanaka, M. Miyanaga *et al.*, "Conceptual Design of Fast Ignition Power Plant KOYO-F Driven by Cooled Yb:YAG Ceramic Laser", Fus. Sci. Technol. **52** (2007) 893-900.

[80] W. Meier, "Systems Modeling Update including Magnetic Deflection", meeting documents of 15th HAPL meeting, General Atomics, San Diego CA, 8-9th August, 2006.

[81] Y. Kamada, N. Ohyama and M. Sugihara, "Various Types of ELMs", J. Plasma Fusion Res. **82** (2006) 566-574 [*in Japanese*].

[82] S. Kajita, S. Takamura, N. Ohno and T. Nishimoto, "Alleviation of Helium Holes/Bubbles on Tungsten Surface by Use of Transient Heat Load", Plasma and Fusion Research **2** (2007) 009.

[83] For example; Y. Sentoku, K. Mima, Z. M. Sheng *et al.*, "Three-dimensional particle-in-cell simulations of energetic electron generation and transport with relativistic laser pulses in overdense plasmas", Phys. Rev. E **65** (2002) 046408.

[84] D. Maisonnier, D. Campbell, I. Cook **et al.**, "Power plant conceptual studies in Europe", Nucl. Fusion **47** (2007) 1524-1532.

[85] M. Murakami and H. Nagatomo, "A new twist for inertial fusion energy: Impact ignition", Nucl. Instr. Methods A **544** (2005) 67-75.

Related Presentations and Publications

Original Paper

- T. Goto, Y. Ogawa, Y. Asaoka, R. Hiwatari and K. Okano, "Development of a System Code for an IFE Reactor and Investigation of a Design Regime for a Dry Wall Chamber Concept", Fusion Engineering and Design **81** (2006) 2785-2790.
- Takuya Goto, Daisuke Ninomiya, Yuichi Ogawa, Ryoji Hiwatari, Yoshiyuki Asaoka, Kunihiko Okano, "Design Study of Dry Wall Fast Ignition Laser Fusion Reactor with High Repetition Laser", Fusion Science and Technology **52** (2007) 953-957.

Related Presentation

International Conference

- ○ Takuya GOTO, Yuichi OGAWA, Yoshiyuki ASAOKA, Ryoji HIWATARI, Kunihiko OKANO, "Development of a System Code for an ICF Reactor and Investigation of a Design Regime for a Dry Wall Chamber Concept", The 15th International Toki Conference, PS2-34, Gifu, Japan, December 6-9th, 2005.
- ○ Takuya GOTO, Daisuke Ninomiya, Yuichi OGAWA, Ryoji HIWATARI, Yoshiyuki ASAOKA, Kunihiko OKANO, "Design Study of Dry Wall Fast Ignition Laser Fusion Reactor with High Repetition Laser", The 17th American Nuclear Society Topical Meeting on the Technology of Fusion Energy (TOFE), 164225, Albuquerque, New Mexico, USA, November 12-15th, 2006
- ○ Takuya GOTO, Yuichi OGAWA, Kunihiko OKANO, Yoshiyuki ASAOKA, Ryoji HIWATARI, Youji SOMEYA, "Analysis of a Core Plasma Dynamics and Dry Wall Chamber for Fast-ignition IFE Power Plant", The Fifth International Conference on Inertial Fusion Sciences and Applications (IFSA2007), Kobe, Japan, September 9-14th, 2007.

Conference Presentation

- ○ Takuya GOTO, Daisuke NINOMIYA, Yuichi OGAWA, Kunihiko OKANO, Yoshiyuki ASAOKA, Ryoji HIWATARI, "Development of the System Code for Designing a Fast Ignition Laser Fusion Reactor and Searching of the Feasible Design Regime for a Commercial Plant", 22nd JSPF annual meeting, 02aA27P, Tower Hall Funabori, Tokyo, Japan, November 28th-Dec. 2nd, 2005.
- ○ Takuya GOTO, Yuichi OGAWA, Kunihiko OKANO, Yoshiyuki ASAOKA, Ryoji HIWATARI, "Design Study of Fast Ignition Laser Fusion Reactors with a Dry Wall Chamber and a High Repetition Laser", 6th fusion energy collaborating meeting, 14I21, Toyama International Conference Hall, Toyama, Japan, June 13rd-14th, 2006.
- ○ Takuya GOTO, Daisuke NINOMIYA, Yuichi OGAWA, Kunihiko OKANO, Yoshiyuki ASAOKA, Ryoji HIWATARI, "Design analysis of Fast Ignition Laser Fusion Reactor with Dry Wall Chamber", 23rd JSPF annual meeting, 01aC32P, University Hall, University of Tsukuba, Ibaraki, Japan, November 28th-December 1st, 2006.
- ○ Takuya GOTO, Daisuke NINOMIYA, Yuichi OGAWA, Ryoji HIWATARI, Yoshiyuki ASAOKA4, Kunihiko OKANO, "Design of a Core Plasma and Chamber Wall for Dry Wall Fast Ignition ICF Power Plant", Japan-US Workshop on Fusion Power Plants and Related Advanced Technologies with participation of EU, Kyoto University, Kyoto, Japan, February 5-7th, 2007.
- ○ Takuya GOTO, Daisuke NINOMIYA, Yuichi OGAWA, "Simulation of Fast Ignition by Using 1-D Hydrodynamic Code ILESTA-1D", JPS spring meeting, 18pQC-2, Kohrimoto Campus, Kagoshima University, Kagoshima, Japan, March 18th-21st, 2007.
- ○ Takuya GOTO, Yuichi OGAWA, Ryoji HIWATARI, Yoshiyuki ASAOKA, Kunihiko OKANO, Youji SOMEYA, "Design Study of a Dry Wall Chamber for a Fast Ignition Laser Fusion Reactor", Japan-US Workshop on Heat Removal and Plasma Materials Interactions for Fusion, Fusion High Power Density Components and System, Sarusawa-So, Nara, Japan, July 25-27th, 2007.
- ○ Takuya GOTO, Yuichi OGAWA, Kunihiko OKANO, Yoshiyuki ASAOKA, Ryoji HIWATARI, Youji SOMEYA "Core Plasma Design and Thermal Analysis of Dry wall for Fast Ignition Laser Fusion Reactor FALCON-D", 24th JSPF annual meeting, 29pC09, Egret Himeji, Hyogo, Japan, November 27th-30th, 2007.